國　立　交　通　大　學
光　電　工　程　研　究　所

碩士論文

氮化鎵微米孔矩陣發光二極體
之發光機制研究

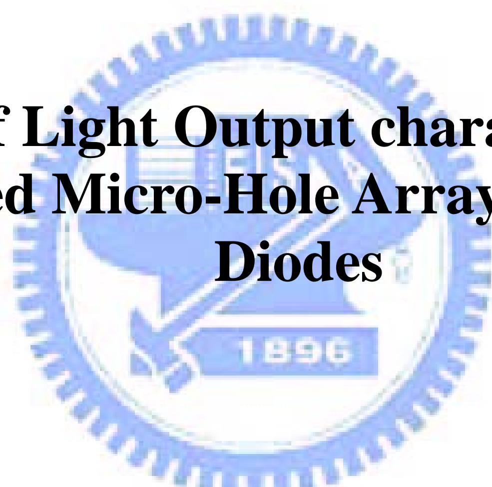

Study of Light Output characteristics of InGaN-based Micro-Hole Array Light-Emitting Diodes

研究生：朱瑞溢
指導教授：郭浩中教授

中華民國九十四年六月

氮化鎵微米孔矩陣發光二極體之發光機制研究

Study of Light Output characteristics of InGaN-based Micro-Hole Array Light-Emitting Diodes

研究生:朱瑞溢　　Student : Jui-Yi Chu

指導教授:郭浩中 教授　　Advisor : Hao-chung Kuo

國 立 交 通 大 學

光電工程研究所

碩 士 論 文

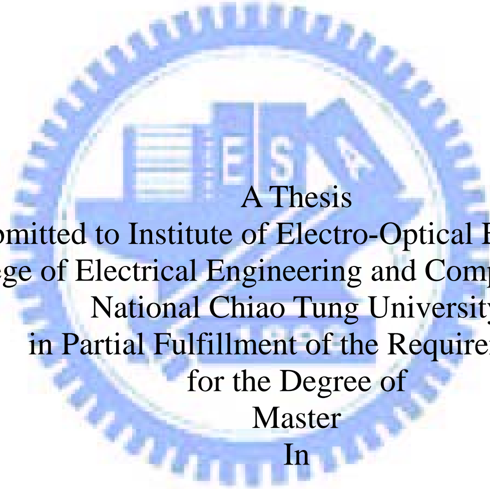

A Thesis
Submitted to Institute of Electro-Optical Engineering
College of Electrical Engineering and Computer Science
National Chiao Tung University
in Partial Fulfillment of the Requirements
for the Degree of
Master
In

Electro-Optical Engineering

June 2005

Hsinchu, Taiwan, Republic of China

中華民國 九十四 年 六 月

氮化鎵微米孔矩陣發光二極體之發光機制研究

研究生:朱瑞溢　　　　　　　　　　　　　指導教授:郭浩中 教授

交通大學光電工程研究所

摘要

本論文討論以自我對準方式製作出的氮化鎵微米孔矩陣發光二極體其電性特徵和發光特性，孔洞直徑分別有 3、7、11 和 15 微米等四種大小，而且傳統的發光二極體也被製作在同樣的試片上做為比較的基楚。在相同 20 毫安培電流操作下發現，元件的電壓值會隨著孔洞直徑的增加而隨著上升，且都略高於傳統的發光二極體；在有相同的主動層面積時，直徑為 7 微米的微米孔矩陣發光二極體有最佳化的輸出功率，比傳統發光二極體提升了 36%。又從失去面積佔整體主動層面積比例(γ)來分析，發現當γ為 6%時，製作微米孔矩陣於發光二極體上對增加輸出功率有最大的增益;而當γ大於 28%時，微米孔矩陣發光二極體的輸出功率開始出現比傳統發光二極體弱的情況。從模擬和實驗二方面對氮化鎵微米孔矩陣發光二極體得到最佳化設計。

之後我們將微米孔矩陣應用於大面積的發光二極體上，並且比較用鎳/金和氧化銦錫二種不同的透明電極在大面積微米孔矩陣發光二極體上的影響。結果發現用氧化銦錫當做透明電極的大面積微米孔矩陣發光二極體和用鎳/金當透明電極的大面積微米孔矩陣發光二極體比較，在相同的孔洞大小時元件的阻值都比較小，且發生輸出光功率出現衰退的電流值都比較高。量測它們的遠場分佈發現，製作微米孔矩陣並不會影響發光二極體的發散角，且發散角的角度分佈在 75°到 80°之間。

Study of Light Output characteristics of InGaN-based Micro-Hole Array Light-Emitting Diodes

Student: Jui-Yi Chu Advisor: Dr. Hao-chung Kuo

Institute of Electro-Optical Engineering

National Chiao Tung University

Abstract

GaN-based micro-hole array LEDs, with hole diameter= 3、7、11 and 15 μm, were fabricated with self-aligned technique. The electrical and light output properties of the micro-hole array LEDs are studied and compared that of the conventional broad-area (BA) LEDs. The forward bias voltage, VF, of the GaN-based micro-hole array LEDs at a driving current of 20 mA increases with d and slightly exceeds that of the conventional BA LEDs. The light output from the micro-hole array LEDs was over 36% grater than that from conventional LEDs with the same device areas. Besides, the enhancement factor of light output from the experimental data decreases as γ increases above 6% (d > 7 μm) and no enhancement is observed from the micro-hole array LEDs at γ > 28%. The optimal design for the GaN-based micro-hole array LEDs are achieved in this work by the experiment and simulation methods.

Furthermore, the optimal design of micro-hole array is used on the GaN-based large-area LEDs. Two kinds of electric conductive material of ITO and Ni/Au are used as the transparent contact layer to the GaN-based large-area micro-hole array LEDs. The results showed that the transparent contact layer of ITO not only decreased the device resistance but also extend the roll-over current. From the emission far-field pattern of LEDs, we found that the micro-hole array on LEDs have little influence on the far field angle. At FWHM, the far field angles are in the range of 75° ~ 80°.

誌謝

回首這兩年的研究生涯，首先感謝王興宗教授與郭浩中教授在研究方面諄諄教誨，讓我學習到研究應有的態度及方法，使我獲益良多。

特別感謝薛道鴻學長這兩年來在實驗上的教導及提供寶貴的意見，給予我在實驗思考上許多的協助。學弟剛帆協助我順利完成實驗；感謝忻宏、亞銜、小強、小朱、詒安學長和芳儀學姊在實驗上的教導與協助；裕鈞、文燈、薏婷、敏瑛、永昌、國峰、傳煜等碩二同學，因為你們，讓我的碩士生活更加有趣，還有其他碩一的學弟妹們，謝謝你們的幫忙。另外，也要感謝一起在新竹讀書的大學同學們，謝謝你們又陪我度過兩年的時光。

最後，我要感謝我的家人，因為你們的支持，讓我能夠順利完成學業，謝謝你們！

Contents

摘 要 i

Abstract.. ii

誌 謝 iii

Contents iv

List of Tables v

List of Figures vi

Chapter 1 Progress in GaN-based Micro-Structure LEDs..1

Chapter 2 Optical property of LEDs and Experiment instrument..................................7

2-1 Theorem on optical properties of semiconductor LEDs......................................7

2-2 The light escape cone..9

2-3 Probe station and spectrum measurement system..11

2-4 Simulation software – TracePro...12

Chapter 3 Simulation Design of Micro-hole Array LEDs by Tracepro...........................15

3-1 Design and Simulation of μ-Hole Array LEDs..16

Chapter 4 Fabrication and Discussion of Micro-hole Array LEDs................................20

4-1 Fabrication of GaN-Based Micro-Hole Array LEDs..20

4-2 Characteristics of GaN-Based Micro-Hole Array LEDs....................................21

Chapter 5 Fabrication and Discussion of Micro-Hole Array Large-Area LEDs.............29

5-1 Fabrication of GaN-Based Micro-Hole Array on Large-Are LEDs....................29

5-2 Characteristics of GaN-Based Micro-Hole Array Large-Area LEDs.................30

Chapter 6 Conclusion..40

Reference...41

List of Tables

Table 3-1 Parameters for the light-tracing simulation of micro-hole array LEDs.......17

Table 5-1 Roll-over current for sample A and sample B...33

List of Figures

Fig. 1.1. Schematics of (a) the MQW structure and (b) the MQW microdisks. A top view SEM image of the microdisk structure is shown in (c). [4]...3

Fig. 1.2. Temperature dependence of the A-exciton decay lifetime (τ) up to 100K. Open squares represent the MQWs and closed triangles represent the microdisks...........3

Fig. 1.3. Optical microphotographs of (a) 16 ×16 micro-LED array (the image is 0.9 mm on a side) and (b) 64 × 64 array (2.4 mm on a side)..4

Fig. 1.4. (a) SEM and (b) optical microscope images of one of our interconnected μ-disk LEDs fabricated from InGaN/GaN QW structures. As illustrated in these images, about 200 μ-disk are interconnected and fit into an area of 300×300 μm^2................4

Fig. 1.5. (a) Schematic of μ-disk LEDs based on p-GaN/InGaN/n-GaN QWs. (b) Optical microscope image (top view) of a microdisplay fabricated from an individually addressed m-disk LED array. The dimension of the microdisplay is 0.5×0.5 mm^2 (made up of 10×10 pixels, 12 μm in diameter). [12]..5

Fig. 1.6. (a) Schematics of the design of a microring LED and (b) diagram showing the possible light extraction pathways from a microring geometry................................5

Fig. 1.7. (a) Cross-sectional schematic of the device structure, and (b) microscope image of the operating device showing four pixels turned on at 6 V..6

Fig. 2.1. Band diagram of active region of LEDs...13

Fig. 2.2. Reservoir analogy...13

Fig. 2.3. Probe station measurement instrument setup..14

Fig. 2.4. Image of Tracepro software...14

Fig. 3.1. Diagrams of extraction efficiency for the conventional LEDs.................................17

Fig. 3.2. Irradiance map of a conventional LED with device dimension of 360×250 μm^2 simulated from the Trace Pro program..18

Fig. 3.3. Simulation design and schematic of our micro-hole array LEDs..............................18

Fig. 3.4. Showing the calculation enhancement of light output power from the micro-hole array LEDs (simulation) and the γ, as functions of d..19
Fig. 4.1. Showing the flowchart of the GaN-based micro-hole array LEDs by standard process...24
Fig. 4.2. Showing the flowchart of the GaN-based micro-hole array LEDs by self-aligned process...25
Fig. 4.3. SEM images of the micro-hole array LEDs with hole diameter= 3 μm....................26
Fig. 4.4. (a) Optical microscope image of a 360 μm × 250 μm micro-hole array LED with d = 7 μm. (b) schematic diagram of a representative micro-hole array LED fabricated by photolithography patterning and dry etching...26
Fig. 4.5. Curves of current-voltage (I-V) of micro-hole array LEDs and a conventional BA LED fabricated from the same wafer...27
Fig. 4.6. Light output power of micro-hole array LEDs and a conventional BA LED as functions of injected current density. The insert shows the light output power-current (L-I) curves..27
Fig. 4.7. Showing (a) micro-photograph and (b) emission profile of a micro-hole array LED with d = 7 μm at 1 mA driving current...28
Fig. 4.8. Schematic of light extraction in BA and micro-hole array LEDs..............................28
Fig. 5.1 Setup and schematics of micro-hole array large-area LEDs......................................33
Fig. 5.2 Showing the flowchart of the GaN-based micro-hole array on large-area LEDs by self-aligned process...34
Fig. 5.3. Optical microscope image of micro-hole array on large-area LED with *d* = 50 μm...35
Fig. 5.4. Curves of current-voltage (I-V) of sample A and a conventional BA LED fabricated from the same wafer...35

Fig. 5.5. Curves of current-voltage (I-V) of micro-hole array on large-area LEDs and a conventional BA LED fabricated from the same wafer..36
Fig. 5.6. VF Comparison of sample A and sample B at current= 300 mA 36
Fig. 5.7. Light output power-current curves of sample A and a conventional BA LED fabricated from the same wafer...37
Fig. 5.8. Light output power-current curves of micro-hole array on large-area LEDs and a conventional BA LED fabricated from the same wafer..37
Fig. 5.9. Light output power of micro-hole array LEDs and a conventional BA LED as functions of injected current density...38
Fig. 5.10. Emission profile of a micro-hole array on large-area LED with d = 50 μm at 20 A/cm^2 driving current...38
Fig. 5.11. Far field pattern of micro-hole array on large-area LEDs.......................................39

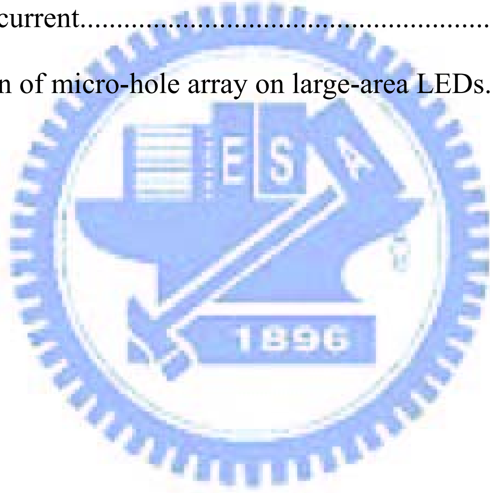

Chapter 1

Progress in GaN-based Micro-Structure LEDs

Recent progresses in electro-optical systems demand drastic increases in the degree of integration of photonic and electronic devices for large-capacity and ultrahigh-light output and information processing. Device size has to be scaled down to nanometric dimensions to meet this requirement, which will become even stricter in the feature. The success of the III-nitride light emitters, including blue light-emitting diodes (LEDs) and laser diodes (LDs) is encouraging for the investigation of microcavity lasers and micro-LEDs. New physical phenomena and properties begin to dominate as device size approaches the wavelength of light, including modified spontaneous emission, enhanced quantum efficiency, emission lifetime, the spectral linewidth, enhanced quantum efficiency, and reduced lasing threshold in microcavities, all of which warrant fundamental investigations [1-3]. In 1997s, the optical properties of GaN/AlGaN multiple quantum well microdisks had been studied, which demonstrate strong enhancement of the transition intensity and lifetime in microdisk structures as shown in Fig. 1.1 and Fig. 1.2 [4]. Optical resonance modes in GaN pyramid microcavities and in III-nitride multiple quantum well microdisk/microring cavities were observed in 1998 and 1999, respectively [5-7]. Recently, the development of microdisplays has mainly focused on liquid crystal (LC), LC on silicon [8], and organic light-emitting diode (OLED) technologies [9]. Microdisplays are small displays that are of such high resolution that they can only be viewed or projected with lenses or mirrors.

The microsize LEDs and lasers provide benefits over edge emitters including the ability to fabricate arrays of individually controllable pixels on a single chip and enhanced quantum efficiency. Recently, H. W. Choi and H. X. Jiang *et al* have demonstrated a lot of III-nitride-based microsize optoelectronics such as matrix-addressable InGaN-based microdisplays (Fig. 1.3), GaN microdisk LEDs (Fig. 1.4), III-nitride blue microdisplays (Fig. 1.5), InGaN microring LEDs and high-density matrix-addressable AlInGaN-based 368-nm microarray LEDs etc (Fig. 1.6 and 1.7) [10-14]. A major imitation to the external quantum efficiency lies in the extraction efficiency of light from the device mesa structure. Such devices are opening up improvements in white LEDs for solid-state lighting applications, and are also expected to offer wide applicability in areas including high-density data storage, chemical and biological sensing devices, in sterilizers and as exposure tools for photolithography. In a commercial photolithographic exposure system, to take one example, both the ultraviolet light source, which is currently typically a mercury lamp or a laser, and a

mask for each pattern in a semiconductor device, are essential to the microfabrication. Since the light source and the mask are independent, it is not possible to correct any device failure due to a design error without making a new mask. In a word, the microsize LEDs have advantages of easy coupling to optical fibers and follow the integration of a dense two-dimensional array onto a single chip.

Many groups have reported high-performance GaN-based micro-disk and micro-ring LEDs [15]-[19]. These μ-LEDs are generally accepted to have greater light output efficiencies than their broad-area (BA) conventional LED counterparts because the (re)absorption of light is reduced on the micrometer scale. Additionally, their greater extraction efficiency relative to the BA devices is attributable to the scattering of light from the etched sidewall surfaces and the great increase in the surface areas of the μ-LEDs [15]-[17]. However, the decline in the area of light-generation of the μ-LEDs may importantly affect their light output performance. This work focuses on the design, fabrication, and characteristics of InGaN-based LEDs μ-hole array LEDs. The effects of the decline in the area of the active region on light output by μ-hole array LEDs were also investigated in detail. This research consists of six chapters. In the chapter 2, we introduce theorem on optical property of semiconductor LEDs、the setup of measurement system and the simulation software TracePro we used in modeling the light extraction of our device and. In chapter 3, we focus on the simulation design of the micro-hole array LEDs. In chapter 4, the fabrication and characteristics of micro-hole array LEDs are introduced and we also compare simulation result with experimental data. Furthermore, we apply the micro-hole array on large-area LEDs and the results will be discussed in chapter 5. Finally, our conclusions and future work are mentioned in the chapter 6.

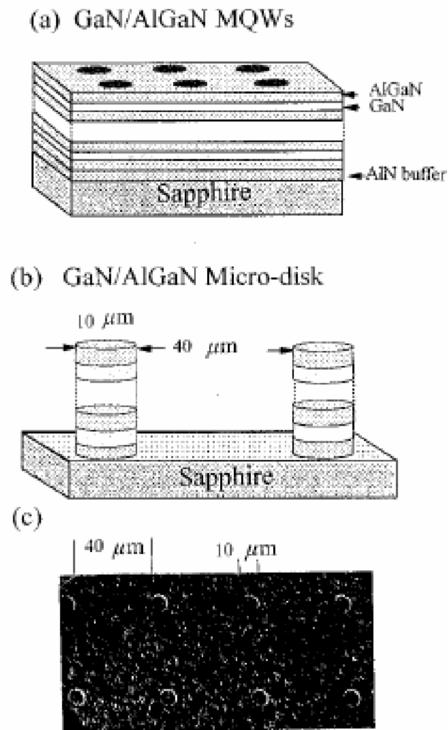

Fig. 1.1. Schematics of (a) the MQW structure and (b) the MQW microdisks. A top view SEM image of the microdisk structure is shown in (c). [4]

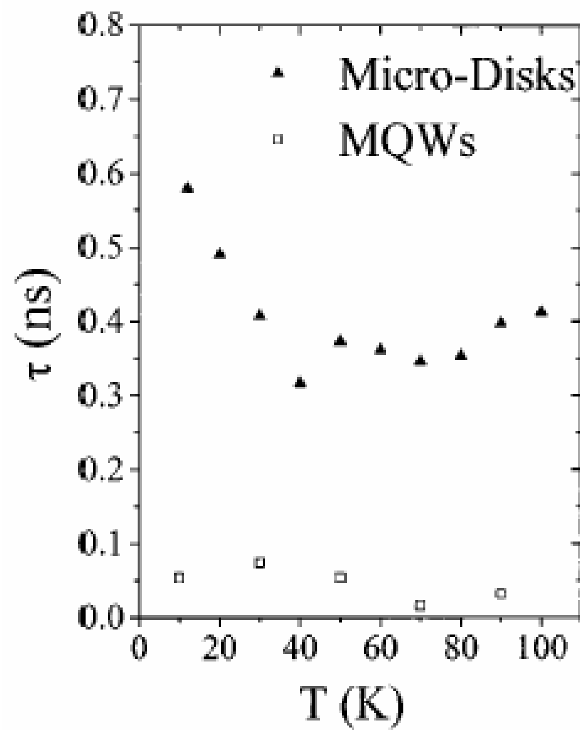

Fig. 1.2. Temperature dependence of the A-exciton decay lifetime (τ) up to 100 K. Open squares represent the MQWs and closed triangles represent the microdisks.

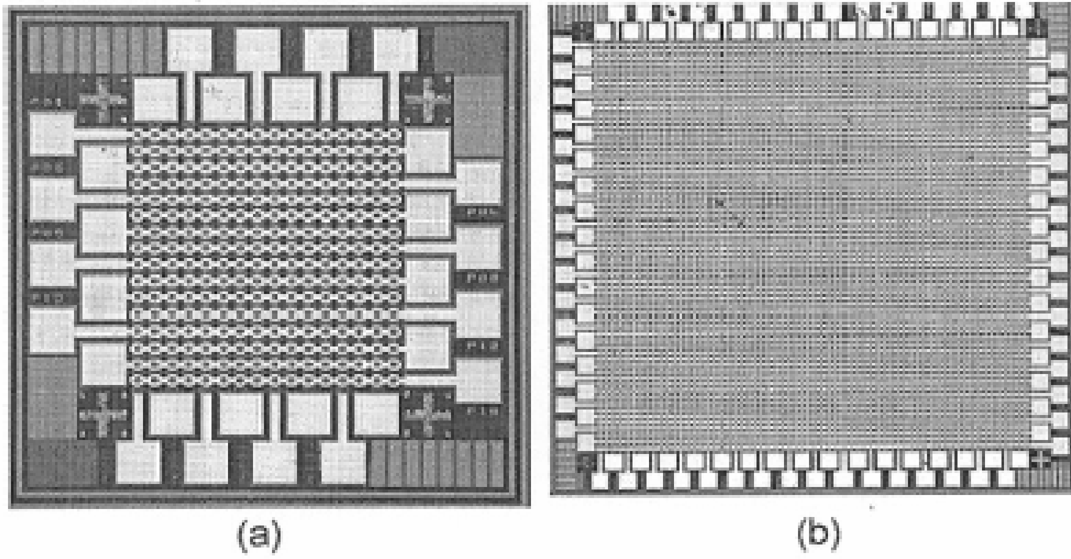

Fig. 1.3. Optical microphotographs of (a) 16 ×16 micro-LED array (the image is 0.9 mm on a side) and (b) 64 × 64 array (2.4 mm on a side).

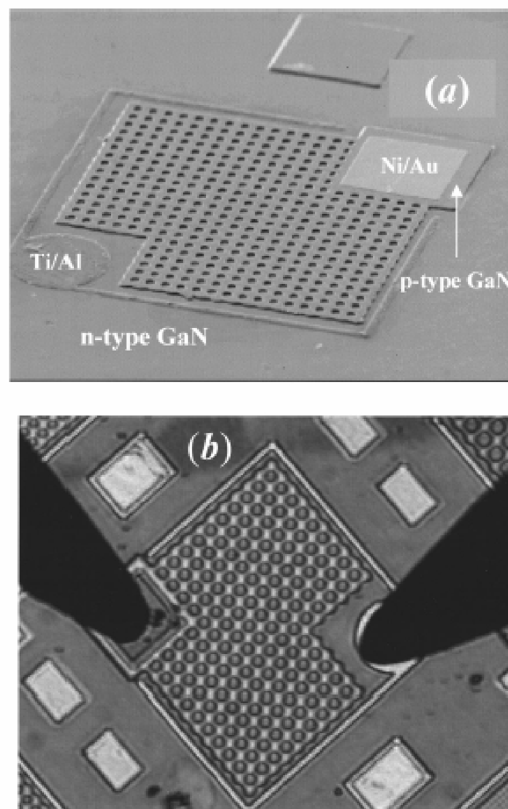

Fig. 1.4. (a) SEM and (b) optical microscope images of one of our interconnected μ-disk LEDs fabricated from InGaN/GaN QW structures. As illustrated in these images, about 200 μ-disk are interconnected and fit into an area of 300×300μm^2.

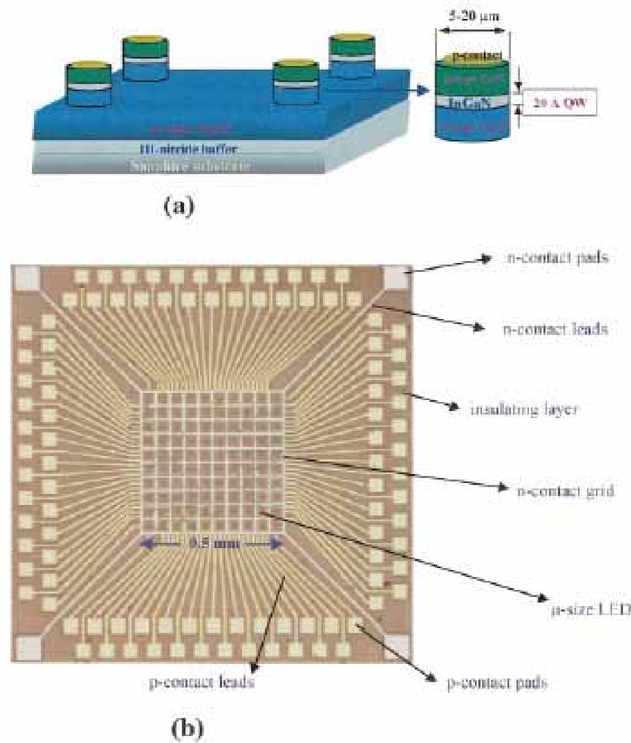

Fig. 1.5. (a) Schematic of μ-disk LEDs based on p-GaN/InGaN/n-GaN QWs. (b) Optical microscope image (top view) of a microdisplay fabricated from an individually addressed m-disk LED array. The dimension of the microdisplay is $0.5 \times 0.5\ mm^2$ (made up of 10×10 pixels, 12 μm in diameter). [12]

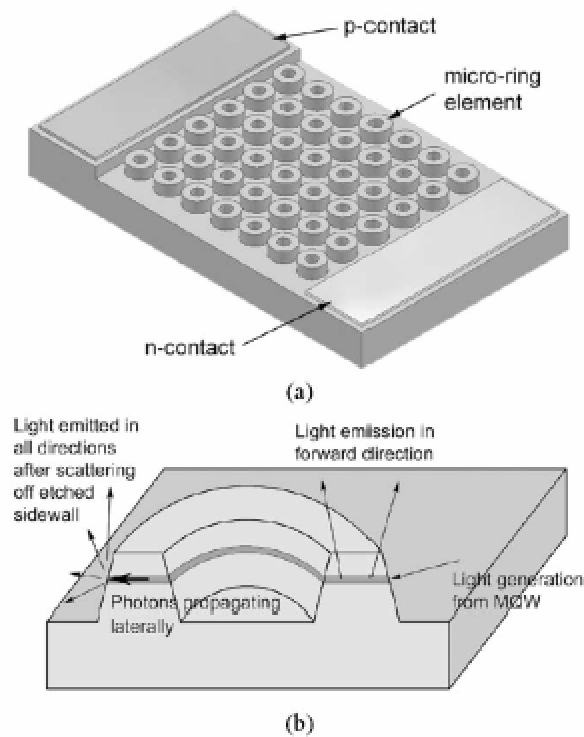

Fig. 1.6. (a) Schematics of the design of a microring LED and (b) diagram showing the possible light extraction pathways from a microring geometry.

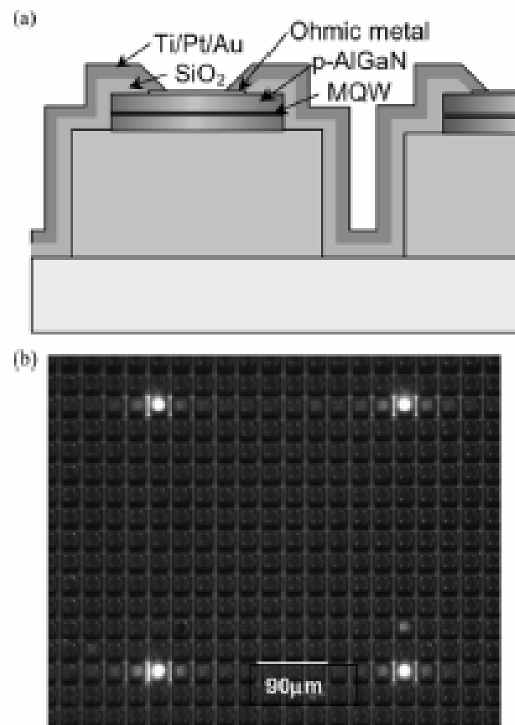

Fig. 1.7. (a) Cross-sectional schematic of the device structure, and (b) microscope image of the operating device showing four pixels turned on at 6 V.

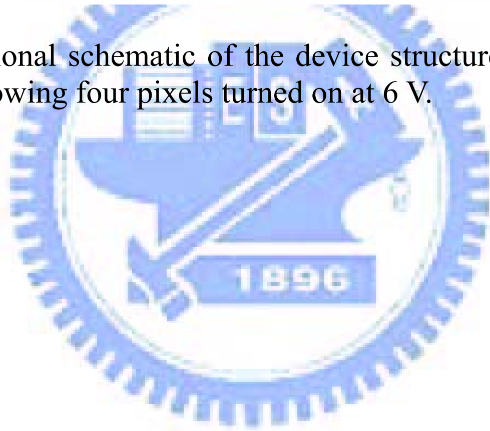

Chapter 2

Optical property of LEDs and instrument

The chapter begins by developing a reservoir model for a flow of charge into double-heterostructure active regions and its subsequent recombination. Recombination mechanism is determined by electron-hole recombination at quantum well generates photons for light emission. For this we describe the phenomenological approach to light emitting diode first. Additionally, the limit on extraction efficiency constrained by critical angle was also shown in the second section.

In the next section, we will mention our electrical measurement system, including of probe station、Keithley 238 CW current source、New Port 1835-C optical meter and spectrum analyzer. We use this system to measure the L-I-V curves、wavelength and near field image of our devices.

Finally, we will introduce the simulation software, TracePro, used in modeling the circumstances of light radiation from LEDs. This software is a ray tracing program that accounts for flux or light power in optical system and is widely used to model: illumination systems, camera systems and projection systems et al.

2-1 Theorem on optical properties of semiconductor LEDs

The proposition considers the current injected into LEDs, and suggests it is desirable to have all of it contributes to electrons and holes which recombine in the active region. Since the definitions of the active region and the internal quantum efficiency, η_i, are so critical to further analysis. Active region, evolved into lowest band-gap region, is where recombining carriers contribute to photon emission. Band diagram of active region, includes separate confinement hetero-structure (SCH) band-gap region, illustrated in Figure 2-1. Internal quantum efficiency, η_i, is the fraction of terminal current that generates carriers in the active region. It is important to realize that includes all of the carriers that are injected into active region, not just carriers that recombine induce radiating at the desired transition energy.

The carrier density, n, in the active region is governed by a dynamic process. In fact, we could compare the process of a certain steady-state carrier density in the active region to that a reservoir analogy, which is being simultaneously filled and drained, in a certain water level. This is shown schematically in Figure 2-2. For the double heterostructure active region, the injected current provides a generation term and various radiative and nonradiative recombination processes as well as carrier leakage provides recombination term. Thus, rate equation is determined as

$$\frac{dn}{dt} = G_{gen} - R_{rec} \tag{2-1}$$

where G_{gen} is the rate of injected electrons and R_{rec} is the rate of recombining electrons per unit volume in the active region. There are $\eta_i I/q$ electrons per second being injected into the active region. V is the volume of the active region.

The recombination process is accompanied with spontaneous emission rate, R_{sp}, and a nonradiative recombination rate, R_{nr}, depicted in Figure 2-2. Carrier leakage rate, R_l, must be occurred at the transverse and/or lateral potential barrier are not sufficiently high. Total recombination rate is expressed as below

$$R_{rec} = R_{sp} + R_{nr} + R_l \tag{2-2}$$

where the first three terms on the right refer to the natural carrier decay processes.
It is common to describe the natural decay processes by a carrier lifetime, τ. In the absence of photon generation term, the rate equation for carrier decay is, $dn/dt = n/\tau$, where $n/\tau = R_{sp} + R_{nr} + R_l$, by comparison to Eq. (2-2). This rate equation defines τ. Besides, this natural decay can be expressed in a power series of the carrier density, n, since each of the terms depends upon the existence of carriers. Besides, we can rewrite Eq. (2-2) as

$$R_{rec} = Bn^2 + \left(An + Cn^3\right)$$

where as the grouping suggests that $R_{sp} \propto Bn^2$ and $R_{nr} + R_l \propto \left(An + cn^3\right)$ The coefficient B is called the bimolecular recombination coefficient. The carrier rate equation in equivalent be expressed as

$$\frac{dn}{dt} = \frac{\eta_i I}{qV} - \frac{n}{\tau} \tag{2-3}$$

The spontaneous photon generation rate per unit volume is exactly equal to the spontaneous electron recombination rate, R_{sp}, since by definition every time an electron-hole pair recombines radiatively, a photon is generated. Under steady-state conditions ($dn/dt = 0$), the generation rate equals the recombination rate, i.e.,

$$\frac{\eta_i I}{qV} = \frac{n}{\tau} = R_{sp} + R_{nr} + R_l$$

The spontaneously generated optical power, P_{sp}, is obtained by multiplying the number of photons generated per unit time per unit volume, R_{sp}, by the energy per photon, $h\nu$, and the volume of the active region, V. Then

$$P_{sp} = h\nu V R_{sp} = \eta_i \eta_r \frac{h\nu}{q} I$$

where the radiative efficiency, η_r, is defined as

$$\eta_r = \frac{R_{sp}}{R_{sp} + R_{nr} + R_l}$$

Usually, the η_r depends upon the carrier density and the product of $\eta_i \eta_r$ is sometimes referred to as the LED internal efficiency. If we interested in how much power the LED emits into some receiving aperture, P, we must further multiply P_{sp} by the extraction efficiency, η_e, experienced in transmitting photons out of the semiconductor and into the aperture. That is,

$$P = \eta_i \eta_r \eta_e \frac{h\nu}{q} I \tag{2-4}$$

At present, we know the output power of LEDs is dominated by two efficiencies: internal efficiency and extraction efficiency. In order to lifting the LEDs output power, many groups have tried to improve the internal efficiency and extraction efficiency as shown in Eq. (2-4). There are two general methods for attaining high internal efficiency: increasing the radiative recombination probability and decreasing the non-radiative recombination probability. Additionally, many groups showed different ways to improve the extraction efficiency: for instance, shaping LED dies or using current spreading layer.

2-2 The light escape cone

Light generated inside a semiconductor cannot escape from the semiconductor if it is totally internally reflected at semiconductor-air interface. If the angle of incidence of a light ray is close to normal incidence, light can escape from the semiconductor. However, total

internal reflection occurs for light rays with oblique and grazing-angle incidence. Total internal reflection reduces the external efficiency significantly, in particular for LEDs consisting of high-refractive-index materials.

Assume that the angle of incidence in the semiconductor at the semiconductor-air interface is given by φ. Then the angle of incidence of the refracted ray, Φ, can be inferred from Snell's law:

$$n_s \sin\varphi = n_{air} \sin\Phi$$

where n_s and n_{air} are the refractive indices of the semiconductor and air, respectively. The critical angle for total reflection is obtained using Φ= 90°. Using Snell's law, we obtain

$$\sin\varphi_c = \left(\frac{n_{air}}{n_s}\right)\sin 90^o = \frac{n_{air}}{n_s} \qquad (2\text{-}5)$$

The refractive indices of semiconductors are usually quite high. For example, GaN has a refractive index of 2.5. Thus, according to Eq. (2-5), the critical angle for total internal reflection is quite small. In this case, we can use the approximation $\sin\varphi_c \approx \varphi_c$. The critical angle for total internal reflection is then given by

$$\varphi_c = \frac{n_{air}}{n_s} \qquad (2\text{-}6)$$

The angle for total internal reflection defines the light-escape cone. Light emitted into the cone can escape from the semiconductor, whereas light emitted outside the cone is subject to total internal reflection.

Next, we calculate the surface area (A) of the spherical cone with radius *r* in order to determine the total fraction of light that is emitted into the light-escape cone.

$$A = \int_{\phi=0}^{\phi_c} 2\pi r \sin\phi r d\phi = 2\pi r^2 (1 - \cos\phi_c)$$

Let us assume that light is emitted from a point-like source in the semiconductor with a total power of P_{source}. Then the power that can escape from the semiconductor is given by

$$P_{escape} = P_{source} \frac{2\pi r^2 (1-\cos\phi_c)}{4\pi r^2}$$

where $4\pi r^2$ is the entire surface area of the sphere with radius *r*.

The calculation indicates that only a fraction of the light emitted inside a semiconductor can escape from the semiconductor. This fraction is given by

$$\frac{P_{escape}}{P_{source}} = \frac{1}{2}(1-\cos\phi_c)$$

Because the critical angle of total internal reflection for high-index materials is relatively small, the cosine tern can be expanded into a power series. Neglecting higher-than-second-order terms yields

$$\frac{P_{escape}}{P_{source}} = \frac{1}{2}\left[1-\left(1-\frac{\phi_c^{\ 2}}{2}\right)\right] = \frac{1}{4}\phi_c^{\ 2}$$

Using the approximation of Eq. (2-6), we obtain

$$\frac{P_{escape}}{P_{source}} = \frac{1}{4}\frac{n_{air}^{\ 2}}{n_s^{\ 2}}$$

The escape problem is a significant problem for high-efficiency LEDs. In most semiconductors, the refractive index is quite high (＞2.5) and thus only a few percent of the light generated in the semiconductor can escape from a planar LED.

2-3` Probe station and spectrum measurement system

Probe station system was essential instrument for basic characteristics measurement such as I-L (current versus light output), I-V (current versus voltage). Scheme of probe station system, illustrated in Figure 2-3, contained probe station, current source, and power-meter module. Keithley 238 as current source supplies continuous current for light emitting diode and receives relative voltage synchronously. Light output power is measured by Newport power-meter module (model 1835C). With these data, we could plot the trend of L-I-V associated with computer. For accuracy power measurement, an integration sphere was used to pick up whole light output from light emitting diode.

For basic measurement, LED device was placed on platform of probe station and injected bias current with microprobe. We could observe L-I-V information by sweeping bias current injection. Distribution of light output intensity is metered as near-field pattern. Near-field pattern (NFP) is still obtained by specific CCD and traces out results with computer. Beam-view analyzer is useful software we used in taking NFP.

Emission spectrum was measured by Advantec optical spectrum analyzer (OSA). We served a multi-mode fiber bundle on probe close to emission aperture in focus for taking spectra. OSA had small spectrum resolution as 0.1nm for accurately measuring spectrum. Scheme of spectrum measurement system was combined with probe station as Figure 2-3.

2-4 Simulation software – TracePro

TracePro is a comprehensive, versatile software tool for modeling the propagation of light in imaging and non-imaging opto-mechanical systems, as shown in figure 2-4. TracePro is a Monte Carlo ray tracing program that accounts for flux or light power in your optical system, as well as the irradiance or the distribution of light.

In Monte Carlo raytracing, scattering and diffraction are treated as random processes. Instead of propagating a distribution of light, discrete samples of the distribution, or rays, are propagated with BSDFs (Bidirectional Scattering Distribution Functions) used as probability distributions for determining ray directions. Monte Carlo ray tracing has several advantages over finite element methods. A list from [33] includes:

- Geometry can be procedural
- No tessellation is necessary
- It is not necessary to precompute a representation for the solution
- Geometry can be duplicated using instancing
- Any type of BRDF can be handled
- Specular reflections (on any shape) are easy
- Memory consumption is low
- The accuracy is controlled at the pixel/image level

To use TracePro, you set up a model of your optical system within the program including optical and non-optical surfaces, and trace rays through the model. You can set up a model importing from a lens design program like OSLO, from a CAD program via SAT, STP, or IGS files, or by creating the solid geometry directly in TracePro. The model includes not only the geometric data specifying the surfaces and optical material data, but also the radiometric properties of the surfaces, i.e., the absorptance, reflectance, transmittance, and scattering coefficients. Rays propagate through the model with portions of the flux of each ray allocated for absorption, specular reflection and transmission, and scattering. This forms a "tree" of rays. The flux of a ray is reduced at each ray-surface interaction, with its flux being reduced in value each time. This process continues until the flux of the ray falls below a threshold set by you. You can run TracePro ray-traces in Analysis Mode and view the incident illuminance (or irradiance) on any surface in the model

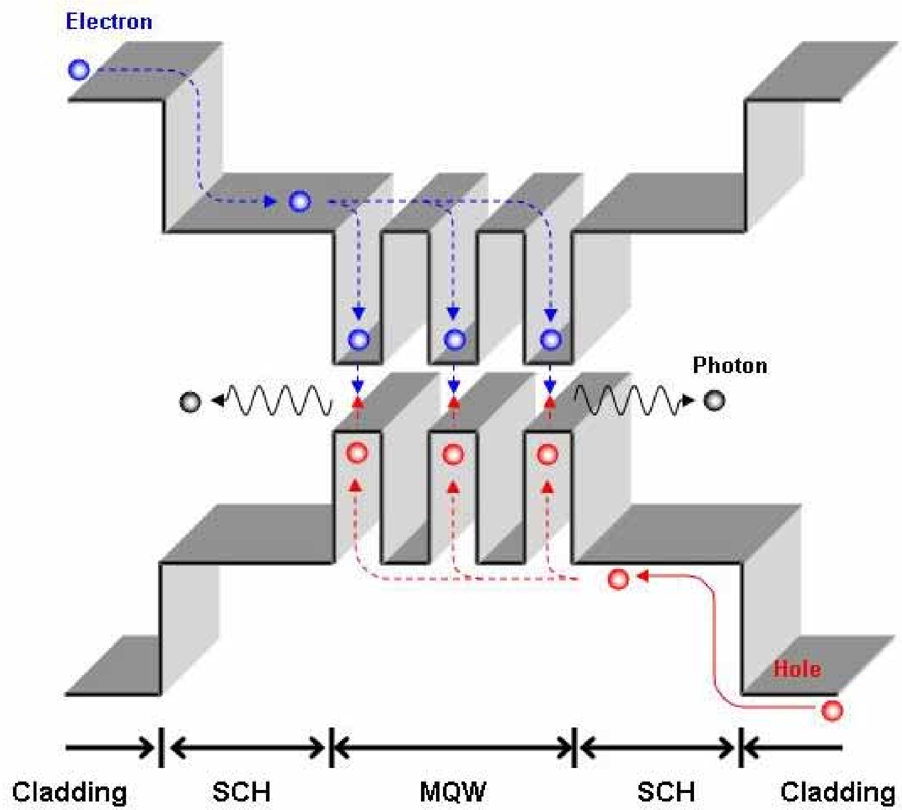

Fig. 2.1. Band diagram of active region of LEDs

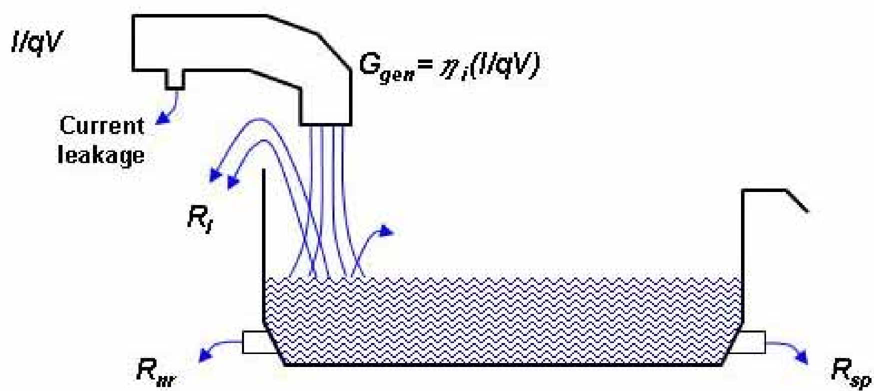

Fig. 2.2. Reservoir analogy

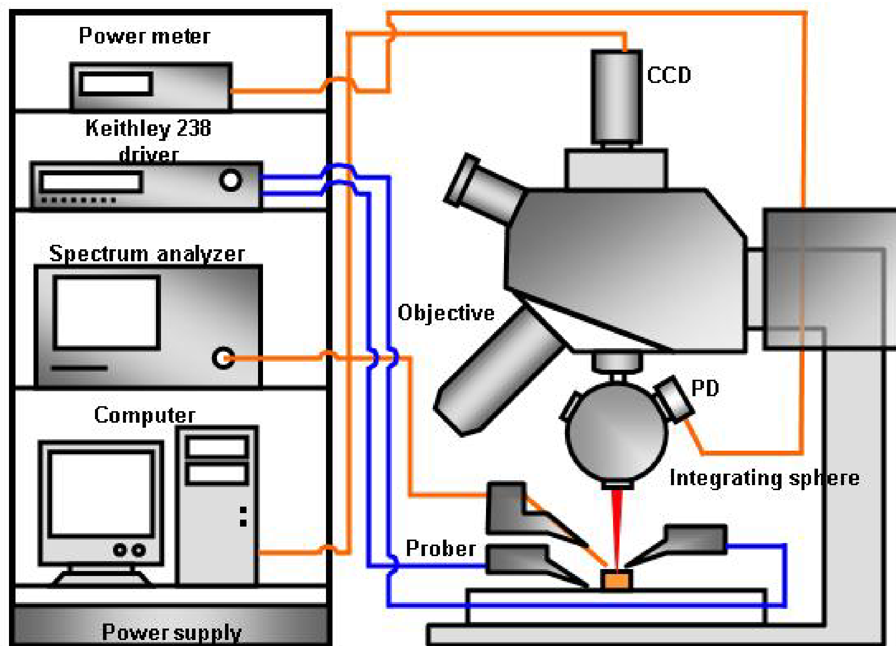

Fig. 2.3. Probe station measurement instrument setup

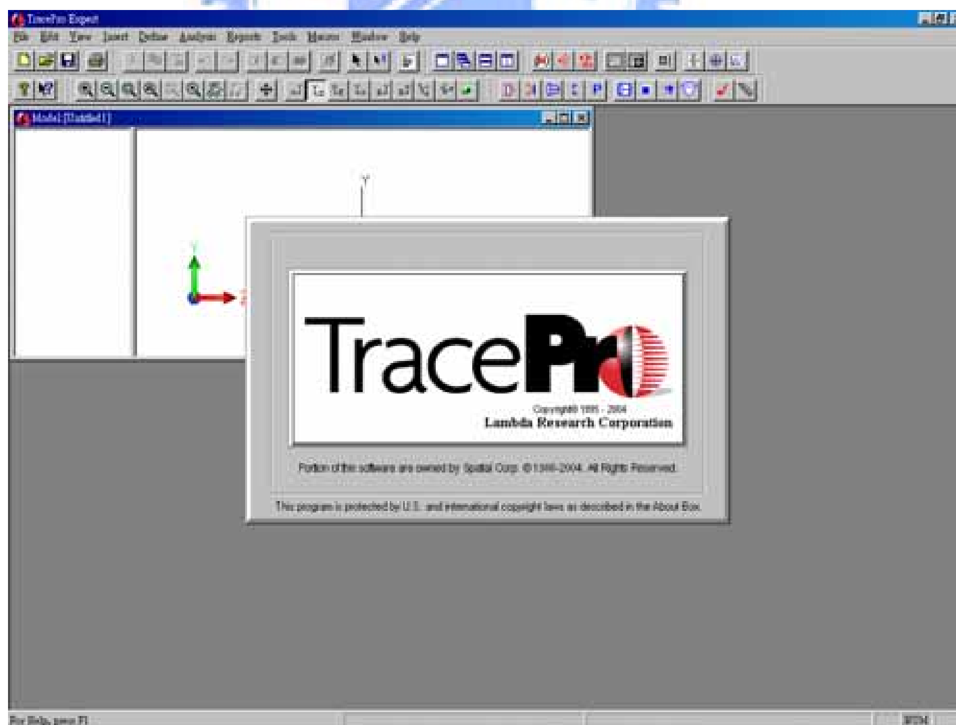

Fig. 2.4. Image of Tracepro software

Chapter 3

Simulation Design of Micro-hole Array LEDs by Tracepro

InGaN-based quantum-well (QW) LEDs are affecting the development of full-color displays, illumination, and exterior automotive lighting over a spectral range from near ultraviolet to green and amber. Devices are grown epitaxially on either sapphire or silicon carbide substrates and their structure contains a single InGaN/GaN QW active region sandwiched between two GaN layers. The absorption coefficient of GaN in the photon-energy range from 2.0 to 3.1 eV is approximately 3×10^2 cm^{-1} [20], so some of the light from the active region is absorbed before it leaves out the devices. Furthermore, approximately $1/(4n^2)$ of the light from the active region radiates through the top and bottom of the devices because of guided modes in which light is totally reflected between the device surface and the air [21]. (The GaN refractive index n is ~2.4) We know emission efficiency of conventional designs is limited by (Fig. 3.1)

- Light transmission through semi-transparent p-metallization,
- Light is reflected at the border between air and device due to the critical angle,
- Absorption of wave-guided light due to multiple pass reflections,
- Light is obscured by bonding pads and wires,
- Large dice are further limited by reduced side light escape.

Recently, III-nitride micro-LEDs (μ-LEDs) have attracted great interest in the area of high-extraction efficiency optoelectronic devices. Many groups have reported high-performance GaN-based micro-disk and micro-ring LEDs [15]-[19]. These μ-LEDs are generally accepted to have greater light output efficiencies than their broad-area (BA) conventional LED counterparts because the (re)absorption of light is reduced on the micrometer scale. Additionally, their greater extraction efficiency relative to the BA devices is attributable to the scattering of light from the etched sidewall surfaces and the great increase in the surface areas of the μ-LEDs. However, the decline in the area of light-generation of the μ-LEDs may importantly affect their light output performance. In this chapter, we focus on the design of the micro-hole array LEDs to have an optimal enhancement of light extraction. Additionally, we discuss the relation between the enhancement of light extraction and the decline in the area of light-generation while fabricating micro-hole array LEDs.

3.1 Design and Simulation of μ-Hole Array LEDs

We set up a sample structure which similar with the wafer we will use in fabricating our device in TracePro software. The structure contains a 4 μm-thick n-GaN; an active layer of five-period $In_{0.2}Ga_{0.8}N$ (3 nm)/GaN (7 nm) QWs; a 50 nm-thick $Al_{0.15}Ga_{0.75}N$ layer, and a 0.25 μm-thick p-GaN. An absorbing plate was placed very close to the p-type GaN layer for imitating the actual environment of measurement.

Fig. 3.2 shows an irradiance map of a conventional GaN-based LED of 360×250 μm^2 simulated from the Trace Pro program. From the Fig. 3.2 we can see that the output-light intensity is observed to be stronger at the edge of the device than that at the center of the device. In this study, the propagation and reflection of light in the devices were examined by applying the ray tracing method in TracePro [22], [23]. The parameters used in all simulations of this work are shown in table 3-1 and the emission power densities in the active regions of all devices were set identical in the simulation. We designed a series of μ-hole array LEDs with hole-diameters of 3, 7, 11, and 15 μm. The spacing between two holes was fixed at 25 μm as shown in Fig. 3.3. Fig. 3.4 plots the factor by which the light output power of various micro-hole array LEDs exceeds that of a conventional BA LED and the ratio (γ) of the etched (lose) light- generating-area of a micro-hole array LED to the mesa area of a conventional BA LED, as functions of d. The enhancement factor of the micro-hole array LED with $d = 7$ μm is ~ 39%. Additionally, in Fig. 3.4, the enhancement factor decreases as γ increases above 6% ($d > 7$ μm) and no enhancement is observed from the micro-hole array LEDs at $\gamma > 28\%$. The large increase in the surface areas efficiently promotes the extraction of the photons that propagate in-plane and the scattering of light off of the sidewalls in the micro-holes. A fraction of the light-generating-area of the micro-hole array LEDs was etched, producing a less active region in the micro-hole array LEDs than that in the conventional BA LEDs. The competition between the improvement in light extraction and the reduction in the area of the active region importantly affects the light output. Accordingly, optimally designing micro-hole array LEDs considerably improves the light output efficiency.

Table 3-1. Parameters for the light-tracing simulation of micro-hole array LEDs

Refractive index (n)		Transmission of Ni/Au (%)	50
GaN	2.5	Total power from the active region (mW)	1
AlGaN	2.2	Absorption coefficient (λ = 460 nm, cm^{-1})	100
Air	1		
Sapphire	1.8		

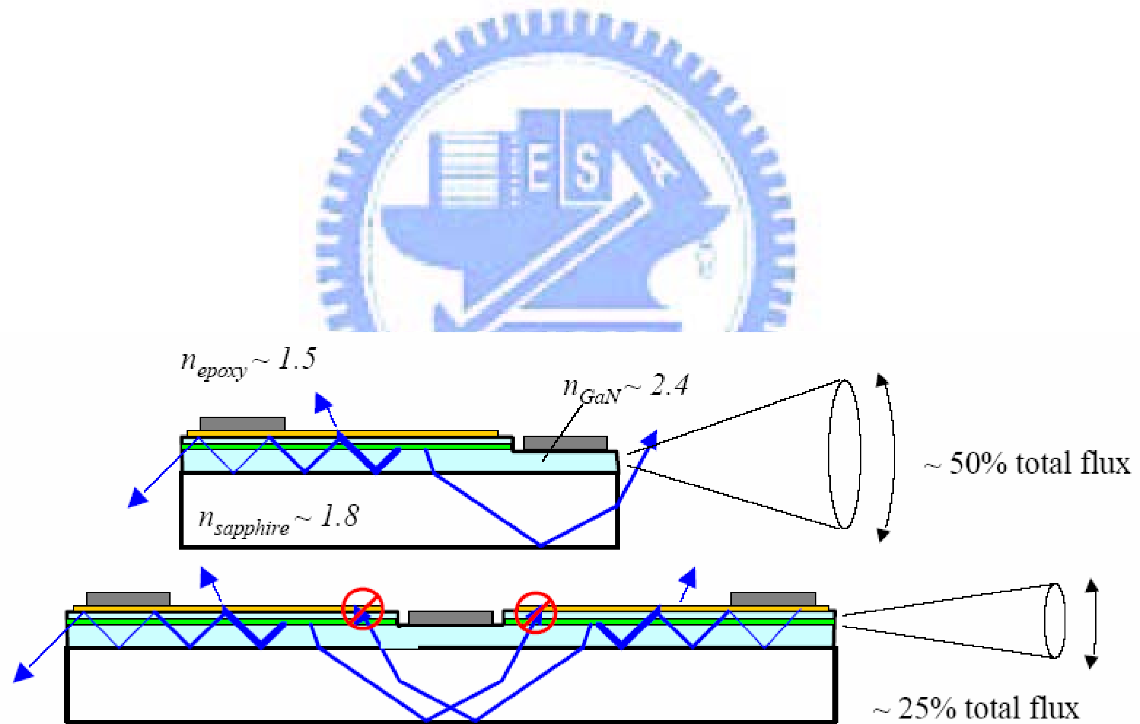

Fig. 3.1. Diagrams of extraction efficiency for the conventional LEDs.

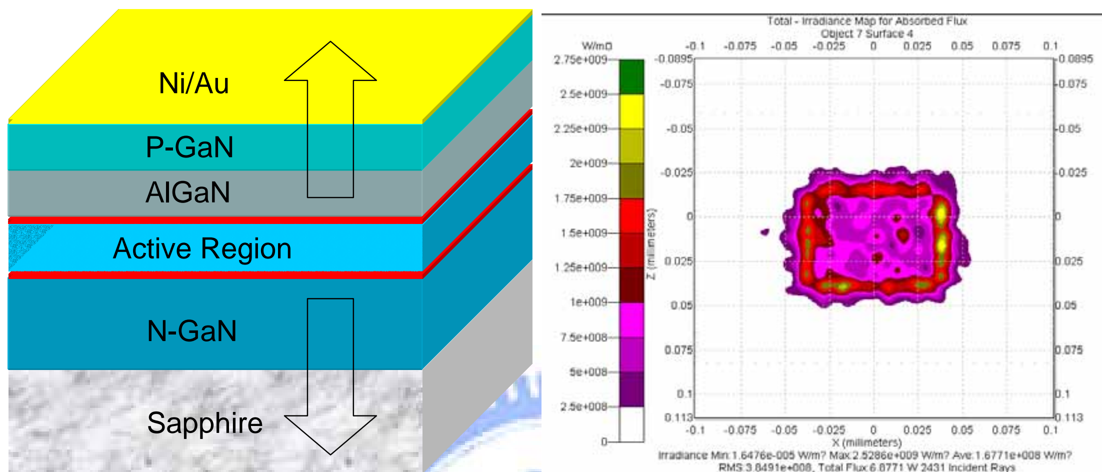

Fig. 3.2. Irradiance map of a conventional LED with device dimension of 360×250 μm^2 simulated from the Trace Pro program.

Mesa size (μm^2)	Spacing (μm)	Hole Diameter (μm)
360x250	25	3
		7
		11
		15
		None

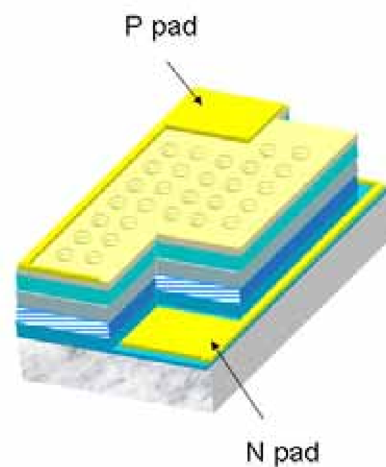

Fig. 3.3. Simulation design and schematic of our micro-hole array LEDs

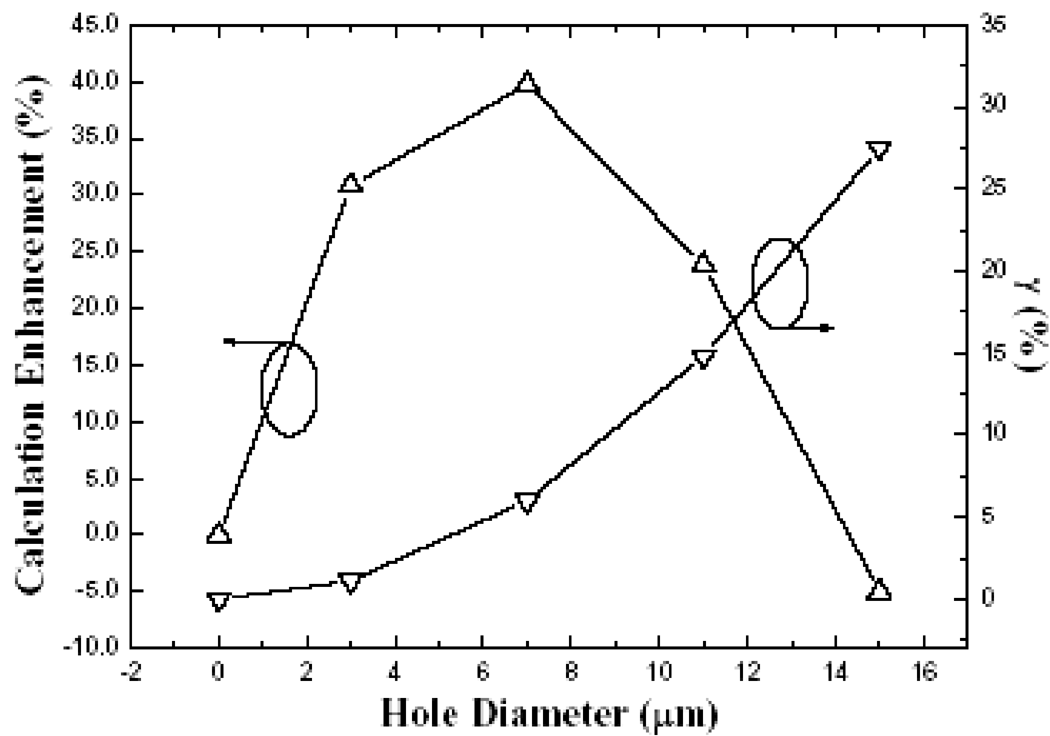

Fig. 3.4. Showing the calculation enhancement of light output power from the micro-hole array LEDs (simulation) and the γ, as functions of *d*.

Chapter 4

Fabrication and Discussion of Micro-hole Array LEDs

In this chapter, our work has stressed the fabrication of micro-hole array LEDs and their electrical characteristics, including of L-I-V、L-J(current density) and near field image were discussed. Finally, we compared our experiment data with the previous simulation results.

4.1 Fabrication of GaN-Based Micro-Hole Array LEDs

The examined samples were grown on c-plane sapphire substrates with a 30 nm-thick GaN nucleation layer by metalorganic chemical vapor deposition. The LED structure contains a 4 μm-thick Si-doped n-GaN; an active layer of five-period $In_{0.2}Ga_{0.8}N$ (3 nm)/GaN (7 nm) QWs; a 50 nm-thick Mg-doped $Al_{0.15}Ga_{0.75}N$ layer, and a 0.25 μm-thick Mg-doped p-GaN. Finally, samples topped with a contact layer of 50-pair Si-doped n^+-$In_{0.23}Ga_{0.77}N$/GaN short-period superlattices rather than high-resistivity p-GaN to reduce the p-contact resistance and improve the current spreading [24]. The wafer growth procedures are reported in detail elsewhere [25].

Figure 4.1 show the processing of the InGaN-based micro-hole array LEDs which began with electron-beam evaporated Ni (5 nm)/Au (8 nm) to form a high-transparency p-type ohmic contact [26]. The holes and the rectangular mesa (360 μm × 250 μm) were fabricated simultaneously by photolithographic patterning, then wet etching of Ni/Au layers individually and inductively coupled plasma (ICP) self-aligned dry etching (SAMCO ICP-RIE 101iPH). The dry etching was performed in a gas mixture of Cl_2/Ar = 10 /25 sccm with an ICP source power of 400 W, a bias power of 40 W and a chamber pressure of 5 mTorr. The effect of pattern-dependent etching on the micro-hole array LEDs is not obvious under these etching conditions. The samples were then etched down to the n-GaN layer with an approximate depth of 1.2 μm. The diameters of the holes were 3, 7, 11, and 15 μm, as determined using a scanning electronic microscope (SEM) measurement. Figure 4.3 is a SEM image shows the dry etching result with micro-hole diameter= 3 μm. Spacing between two holes was fixed at 25 μm. Notably, the procedures for fabricating the micro-hole array LEDs are identical to those for fabricating conventional BA LEDs. Thermal annealing was applied to the p-type contact alloy at 500°C in air for 5 minutes. Finally, the trilayers of Ti/Pt/Au (50 nm/20 nm/200 nm) for p、n-type pad and n-type ohmic contact were deposited. We should note the

evaporation of Ni/Au transparent contact layer and etching mesa were accomplished at the same time, called self-align process, in our fabrication of micro-hole array LED. The comparison of self-align process with the conventional process of LEDs was described as follows:

Figure 4.1 shows the the self-aligned processing of LEDs fabrication and Figure 4.2 shows standard processing of LEDs fabrication. In Figure 4.2, we know standard processing fabrication of LEDs basically includes mesa etching、evaporation of transparent contact layer(TCL)、thermal annealing TCL and evaporation of p、n contact metal. This method includes at least three times photo lithography process; first is defining the mesa size, second is defining the TCL region and third is defining the p、n contact pad region. The second step is usually difficult because the margin between TCL and the mesa side wall is small. If an inaccurate alignment between the TCL and mesa region happens, it will cause a few TCL metal evaporated on the sidewall of the mesa that result in the leakage current. In order to solve this problem, we adopt the self-aligned process in our micro-hole array LEDs fabrication, shown in Figure 4.1, which evaporate the TCL before mesa etching. Thus we can transform one time photo lithography alignment into one wet etching or dry etching of TCL metal process and lower the perplexity of fabricating LEDs.

Fig. 4.4 (a) shows an optical microphotograph of the top of a micro-hole array LED chip with d = 7 μm and Fig. 4.4 (b) schematically depicts a micro-hole array LED. The conventional BA LEDs with the same mesa size (360 μm × 250 μm) were also fabricated from the same wafer for comparison. The probe-station system (Wentworth Laboratories, model: MP2300) is used for electronically characteristic measurements as shown in Fig. 2.3. The typical current-voltage measurements were performed using a high current measure unit (KEITHLEY 238). The light output power was measured using a calibrated power meter with a large Si detector (detector area 10×10 mm^2) approximate 5 mm above the device, collecting the light emitted in the forward direction.

4.2 Characteristics of GaN-Based Micro-Hole Array LEDs

Figure 4.5 plots the current-voltage (I-V) characteristics of the micro-hole array LEDs with different values of d and that of a conventional BA LED fabricated from the same wafer. The devices have unequal area of light-generation, so the insert in Fig. 4.5 plots the current

density-voltage (J-V) (evaluated by taking the ratio of the actual driving currents to their active areas). The forward bias voltage, V_F, at a driving current of 20 mA increases with d (V_F = 3.38, 3.41, 3.57 and 3.80 V for d = 3, 7, 11 and 15 μm) and slightly exceeds that of the conventional BA LED (V_F = 3.28 V). The J-V characteristic is similar to the I-V characteristic in Fig. 4.5. Additionally, the operating voltages of the micro-hole array LEDs marginally exceed those of the conventional BA LED, because of the reduction in the total active area [15], [16], [27] and the presence of a plasma-damage region parallel to the sidewalls within the holes [28]. The holes were fabricated by dry etching; plasma damage occurs on the sidewalls, increasing the surface recombination of the injected electrons and holes.

Figure 4.6 plots the light output-current density (L-J) curves. The micro-hole array LED with d = 7 μm has a light output power of ~ 3.0 mW at 22.2 A/cm^2 (corresponding to a driving current of 20 mA for the conventional BA LED), which is 36% greater than ~ 2.2 mW for the conventional BA LED. Moreover, the light output power of the micro-hole array LEDs decreases as the d increases above 11 μm and the light output power of the micro-hole array LED with d = 15 μm is less than that of the conventional BA LED. The insert in Fig. 4.6 plots the light output-current (L-I) curves. The light output power increases as the d increases, being distinct from the L-J curves. Notably, the L-I curves are similar as the d increases above 7 μm. The light output by an optoelectronic device is governed by the internal quantum efficiency and extraction efficiency. Internal quantum efficiency is a natural property of LEDs; the geometry of the device strongly influences the extraction efficiency. Fig. 4.7 (a) and (b) present the emission image and the intensity profile of a micro-hole array LED with d = 7 μm at an operating current of 1 mA, respectively. A bright luminescence ring is observed at the periphery of the hole, similar to that observed in micro-pillar LEDs [15]. Fig. 4.8 shows the schematic of light extraction of the BA and micro-hole array LEDs. Most of the light propagated in the plane is emitted through the surface of the sidewall, but scattering on the etched sidewall causes some of the light to be extracted from the top surface near the periphery, causing the ring of light to be observed in the emission images, and increasing the light output in the forward direction.

Comparison these experimental data with the previous simulated results, we found that the simulated enhancement factor of the micro-hole array LED with d = 7 μm is ~ 39% and is similar with the experimental values, 36%, slightly exceeding it perhaps because non-radiative recombination on the etched sidewall surfaces of the micro-hole array LEDs. Additionally, the enhancement factor in experimental data decreases as γ increases above 6%

(d > 7 μm) and no enhancement is observed from the micro-hole array LEDs at γ > 28% as we expected in the simulated results.

In summary, highly efficient InGaN-based micro-hole array LEDs were fabricated. Their characteristics were measured and compared with those of conventional BA LEDs fabricated from the same wafer. The light output from the micro-hole array LEDs was over 36% grater than that from conventional LEDs with the same device areas. In particular, microhole array LEDs exhibited the highest enhancement in light output at γ =6% and no enhancement when γ > 28%. These facts are attributable to combination of the enhancement in extraction efficiency by increasing the area of the sidewall surfaces and the reduction of the active areas of the micro-hole array LEDs. Optimally designed InGaN-based micro-hole array LEDs exhibit improved light output efficiently and are candidate for white-light LEDs or high-power/ high-efficiency large-area LEDs.

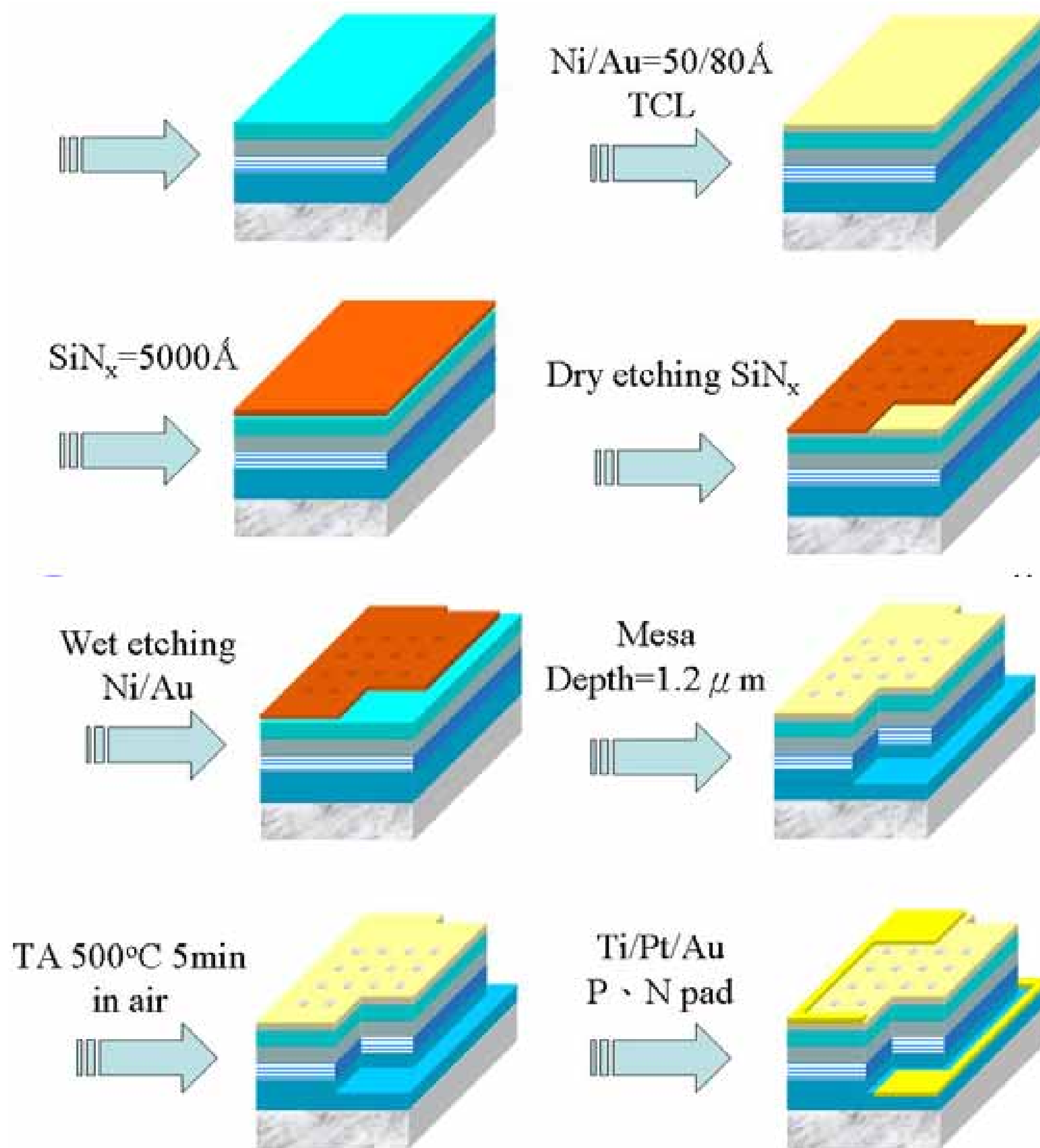

Fig. 4.1. Showing the flowchart of the GaN-based micro-hole array LEDs by standard process.

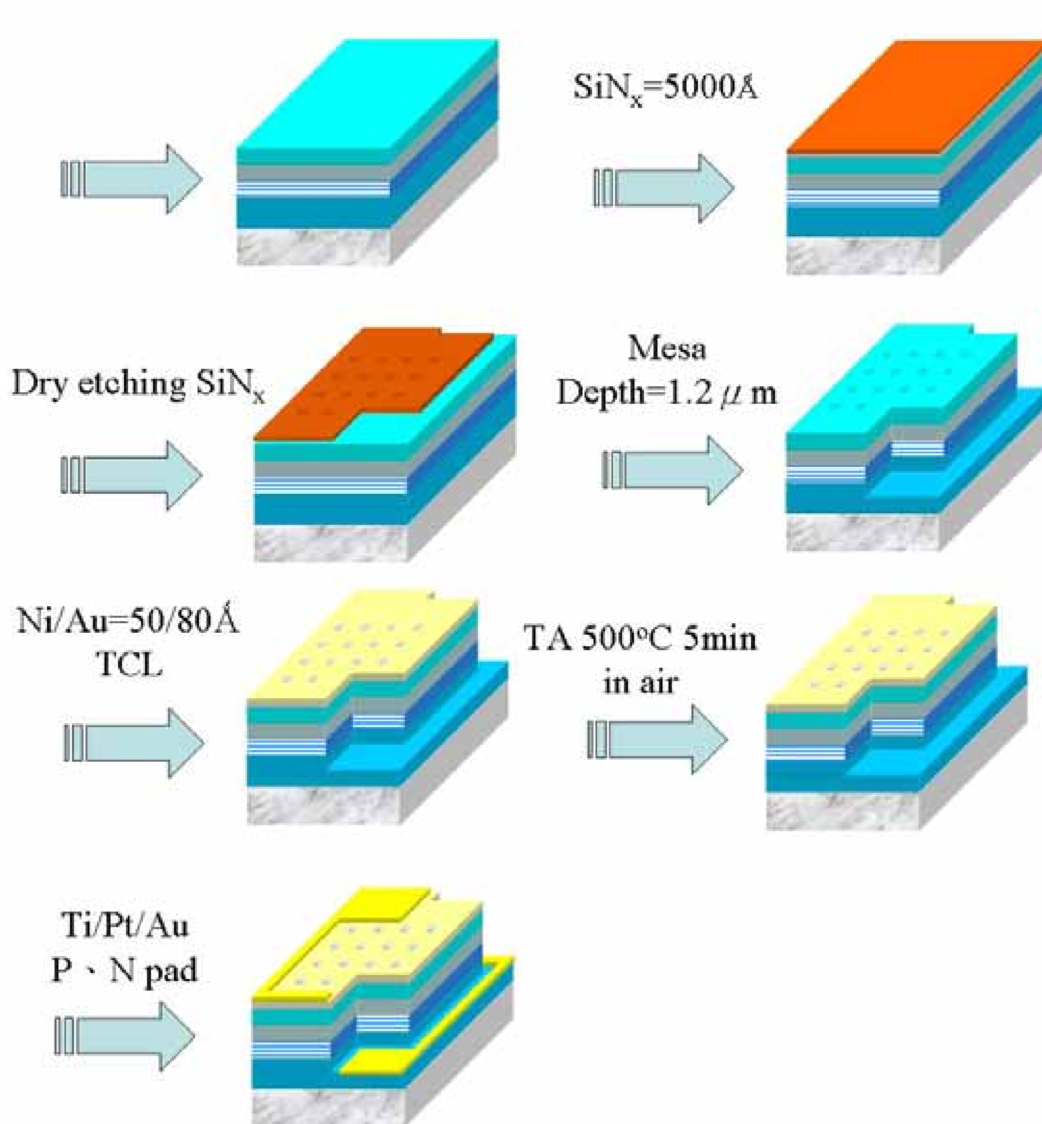

Fig. 4.2. Showing the flowchart of the GaN-based micro-hole array LEDs by self-aligned process.

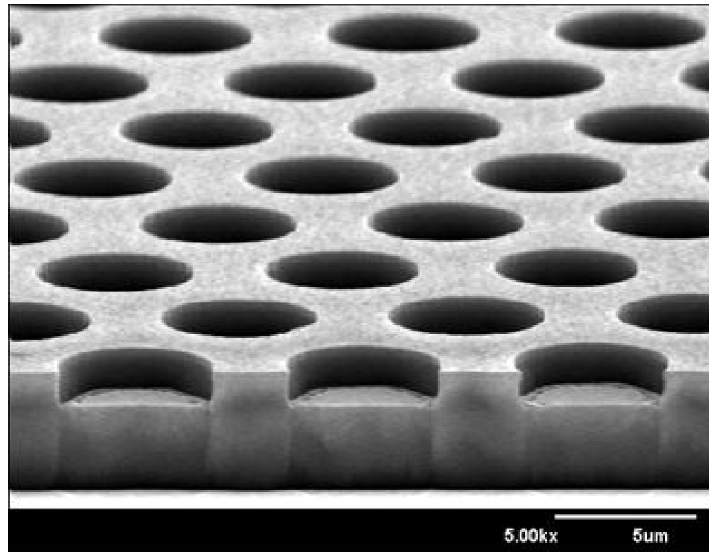

Fig. 4.3. SEM images of the micro-hole array LEDs with hole diameter= 3 μm.

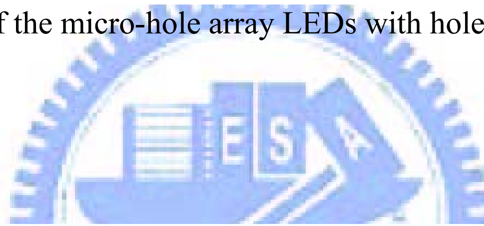

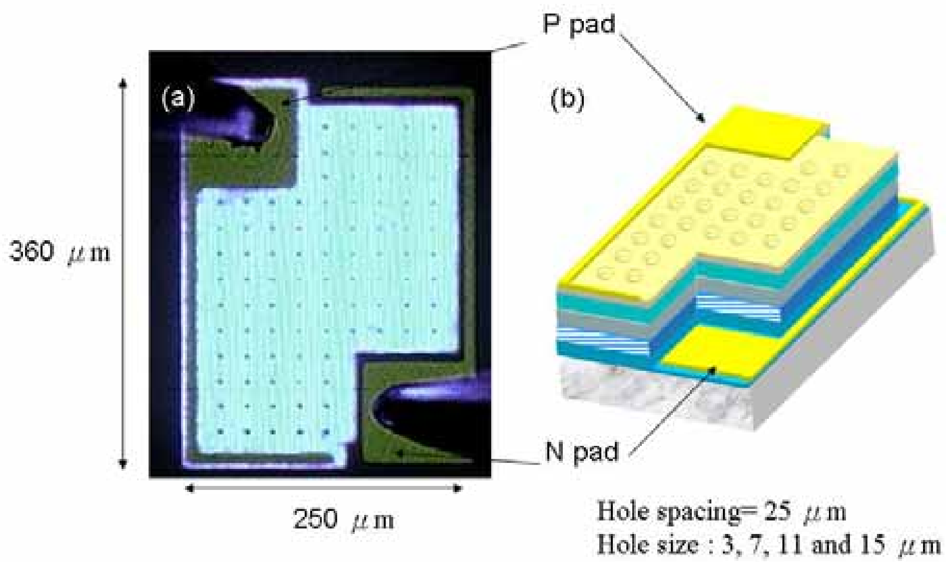

Fig. 4.4. (a) Optical microscope image of a 360 μm × 250 μm micro-hole array LED with d = 7 μm. (b) schematic diagram of a representative micro-hole array LED fabricated by photolithography patterning and dry etching.

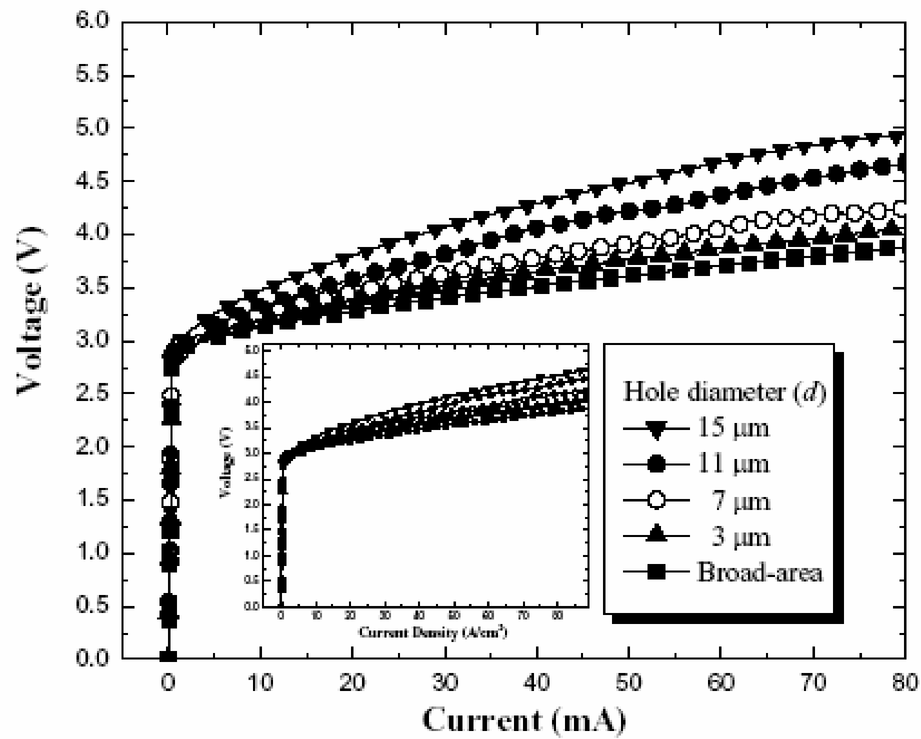

Fig. 4.5. Curves of current-voltage (I-V) of micro-hole array LEDs and a conventional BA LED fabricated from the same wafer.

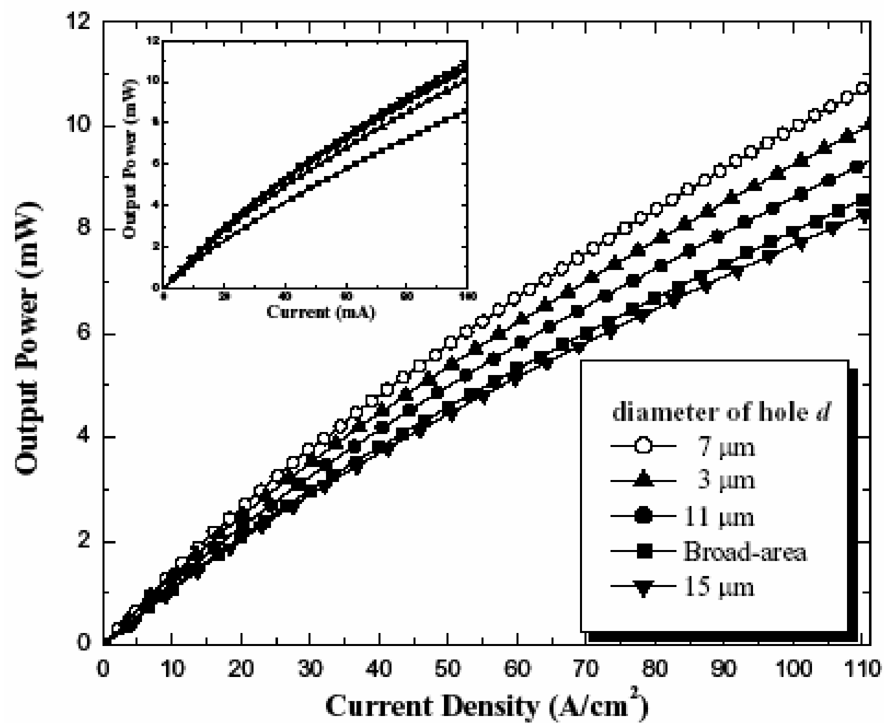

Fig. 4.6. Light output power of micro-hole array LEDs and a conventional BA LED as functions of injected current density. The insert shows the light output power-current (*L-I*) curves.

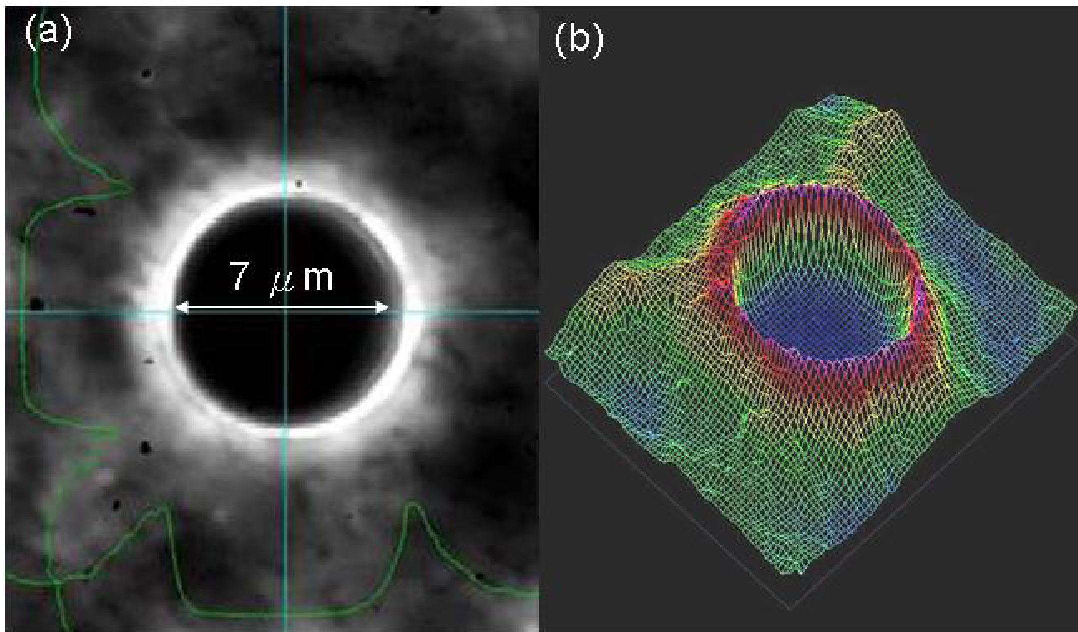

Fig. 4.7. Showing (a) micro-photograph and (b) emission profile of a micro-hole array LED with d = 7 μm at 1 mA driving current.

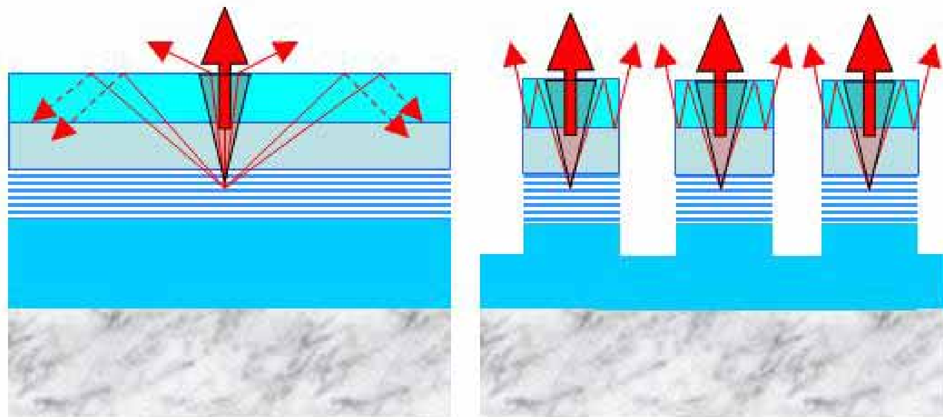

Fig. 4.8. Schematic of light extraction in BA and micro-hole array LEDs.

Chapter 5

Fabrication and Discussion of Micro-Hole Array Large-Area-LEDs

For high power LED application, large-area LEDs is also an important issue. Therefore, we applied the micro-hole array to large-area LEDs with hole-diameter *d*= 10、20、30、40 and 50 μm based on the previous lost active-region ratio, γ, shown in Fig. 5.1. Additionally, two kinds of electric conductive metal of Ni/Au and ITO are used as transparent contact layer to the micro-hole array large-area LEDs and their electrical characteristics are discussed.

5.1 Fabrication of GaN-Based Micro-Hole Array Large-Area LEDs

The examined samples were grown on c-plane sapphire substrates with a 30 nm-thick GaN nucleation layer by metalorganic chemical vapor deposition. The LED structure contains a 4 μm-thick Si-doped n-GaN; an active layer of five-period $In_{0.2}Ga_{0.8}N$ (3 nm)/GaN (7 nm) QWs; a 50 nm-thick Mg-doped $Al_{0.15}Ga_{0.75}N$ layer, and a 0.25 μm-thick Mg-doped p-GaN. Finally, samples topped with a contact layer of 50-pair Si-doped n^{+}-$In_{0.23}Ga_{0.77}N$/GaN short-period superlattices rather than high-resistivity p-GaN to reduce the p-contact resistance and improve the current spreading [24]. The wafer growth procedures are reported in detail elsewhere [25].

We prepared two identical samples, sample A and sample B, to fabricate the micro-hole array large-area LEDs. The only difference between fabrication of sample A and sample B was the transparent contact layer. The schematic flow chart was shown in Fig. 5.2. Sample A began with electron-beam evaporated Ni/Au (50/80 nm) and sample B began with the electron-beam evaporated TIO (300 nm) as the transparent contact layer. The remaining process of fabrication micro-hole array large-area LEDs was the same and described as follows. The holes and the circular mesa (diameter= 1.12 mm and mesa area= 1mm^2) were fabricated simultaneously by photolithographic patterning, then wet etching of transparent contact layer and inductively coupled plasma (ICP) self-aligned dry etching (SAMCO ICP-RIE 101iPH). The dry etching was performed in a gas mixture of Cl_2/Ar = 10 /25 sccm with an ICP source power of 400 W, a bias power of 40 W and a chamber pressure of 5 mTorr. The effect of pattern-dependent etching on the micro-hole array on large-area LEDs is not obvious under these etching conditions. The samples were then etched down to the n-GaN layer with an approximate depth of 1.2 μm. The diameters of the holes were 10, 20, 30, 40

and 50 μm, as determined using a scanning electronic microscope (SEM) measurement. Spacing between two holes was fixed at 60 μm. Notably, the procedures for fabricating the micro-hole array LEDs are identical to those for fabricating conventional BA LEDs. Finally, the trilayers of Ti/Pt/Au (50 nm/20 nm/200 nm) for p、n-type pad and n-type ohmic contact were deposited. Fig. 5.3 shows an optical microphotograph of the top of a micro-hole array LED chip with ITO as the transparent contact layer and *d* = 50 μm. The conventional BA LEDs with the same mesa size (diameter= 1.12 mm and mesa area= 1mm^2) were also fabricated from the same wafer for comparison. The probe-station system (Wentworth Laboratories, model: MP2300) is used for electronically characteristic measurements as shown in Fig. 2.3. The typical current-voltage measurements were performed using a high current measure unit (KEITHLEY 238). The light output power was measured using a calibrated power meter with a large Si detector (detector area 10×10 mm^2) approximate 5 mm above the device, collecting the light emitted in the forward direction.

5.2 Characteristics of GaN-Based Micro-Hole Array Large-Area LEDs

Figure 5.4 and Figure 5.5 plot the current-voltage (*I-V*) characteristics of the sample A and sample B with different values of *d* respectively and that of a conventional BA LED fabricated from the same wafer. Both the forward bias voltage, V_F, at a driving current of 300 mA increases with *d*: V_F = 4.8, 4.95, 5.67, 5.99, 6.15 V for *d* = 10, 20, 30, 40, 50 μm in sample A and V_F = 4.51, 4.75, 4.85, 5.32, 5.48 V for *d* = 10, 20, 30, 40, 50 μm. Additionally, the operating voltages of the micro-hole array large-area LEDs marginally exceed those of their conventional BA LED: V_F = 4.73 V for sample A and V_F = 4.47 V for sample B. This is attributed to the reduction in the total active area [15], [16], [27] and the presence of a plasma-damage region parallel to the sidewalls within the holes [28]. These holes were fabricated by dry etching; plasma damage occurs on the sidewalls, increasing the surface recombination of the injected electrons and holes. Figure 5.6 show the V_F comparison of sample A and sample B at driving current= 300mA. From figure 5.6, we can obviously observe the V_F in sample B was lower than that in sample A with the same *d.*

Figure 5.7 and figure 5.8 plot the light output-current (*L*-I) curves for sample A and sample B respectively. The light output by an optoelectronic device is governed by the internal quantum efficiency and extraction efficiency. Internal quantum efficiency is a natural

property of LEDs; the geometry of the device strongly influences the extraction efficiency. Both the light output power increases as the *d* increases under low current injection. Particularly, some intersection points were found in the L-I curves with increasing injection current. For example, the L-I curve for *d*= 50 μm crossed the L-I curve for broad area LED at 520mA in figure 5.9. The output power rolled over because of the current crowding near the contact pad, leading to heat effect and band-filling. We define the current as roll-over current while the differential of L-I curve equals to zero. Table 5.1 showed the roll-over current for sample A and sample B. From Table 5.1, we found that light output power roll over earlier with the larger *d* while increasing the injection current. Besides, the roll-over currents for sample B were larger than those for sample A with the same *d*.

Figure 5.9 plots the light output-current density (*L-J*) curves for sample B. The micro-hole array LED with *d* = 20 μm has a light output power of ~ 39.3 mW at 378 A/cm^2 (corresponding to a driving current of 350 mA for the conventional BA LED), which is 27.1% greater than ~ 30.9 mW for the conventional BA LED. Moreover, the light output power of the micro-hole array LEDs decreases as the *d* increases above 30 μm and the light output power of the micro-hole array LED with *d* = 50 μm is less than that of the conventional BA LED. Fig. 5.10 presents the emission profile of a micro-hole array on large-area LED with *d* = 50 μm at an operating current density 20 A/cm^2. A bright luminescence ring is observed at the periphery of the hole, equal to that observed in micro-hole array LEDs.

We diced the sample B and made them packaged as TO can form. Fig. 5.11 shows the far field pattern of the micro-hole array on large-area LEDs at 350mA with the intensity normalized. No obvious changes in the far field pattern were shown, far field angle= ±75°~80° at FWHM. Since the enhancement of light extraction is coming from the increasing probability of light extracted from the sidewall, the way that light extracted from the micro-hole array LEDs is the same with the BA LEDs. Therefore, we knew that fabricating micro-hole array on LEDs will not change the far field angle of LEDs and the far field angles are in the range of 75° ~ 80° at FWMA

In summary, InGaN-based micro-hole array on large-area LEDs with two different transparent contact layers were fabricated. Their characteristics were measured and compared with those of conventional BA LEDs fabricated from the same sample respectively. The using ITO as transparent contact layer has shown not only decreasing the resistance of micro-hole

array large-area LEDs but also prolonging the roll-over current. The light output from the micro-hole array on large-area LEDs was over 27% grater than that from conventional LEDs at 378 A/cm^2 with the same device areas. In particular, micro-hole array on large-area LEDs exhibited not enhancement when d = 50 μm. These facts are attributable to combination of the enhancement in extraction efficiency by increasing the area of the sidewall surfaces and the reduction of the active areas of the micro-hole array LEDs. Moreover, the far field pattern measurement showed the fabrication of micro-hole array on large-area LEDs will not change the far field angle of LEDs and the far field angles are in the range of 75° ~ 80° at FWHM.

.

	10 (μm)	20 (μm)	30 (μm)	40 (μm)	50 (μm)	BA LED
Sample A (mA)	None	600	530	485	385	None
Sample B (mA)	None	None	None	550	490	None

Table 5.1. Roll-over current for sample A and sample B.

Mesa size (mm^2)	Spacing (μm)	Hole Diameter (μm)	γ (%)
1	60	10	3
		20	6
		30	15
		40	28
		50	35
		None	None

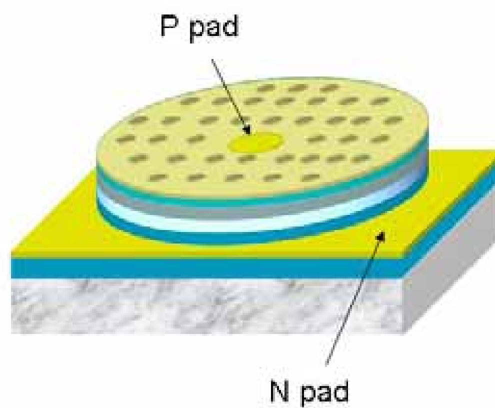

Fig. 5.1 Setup and schematics of micro-hole array large-area LEDs

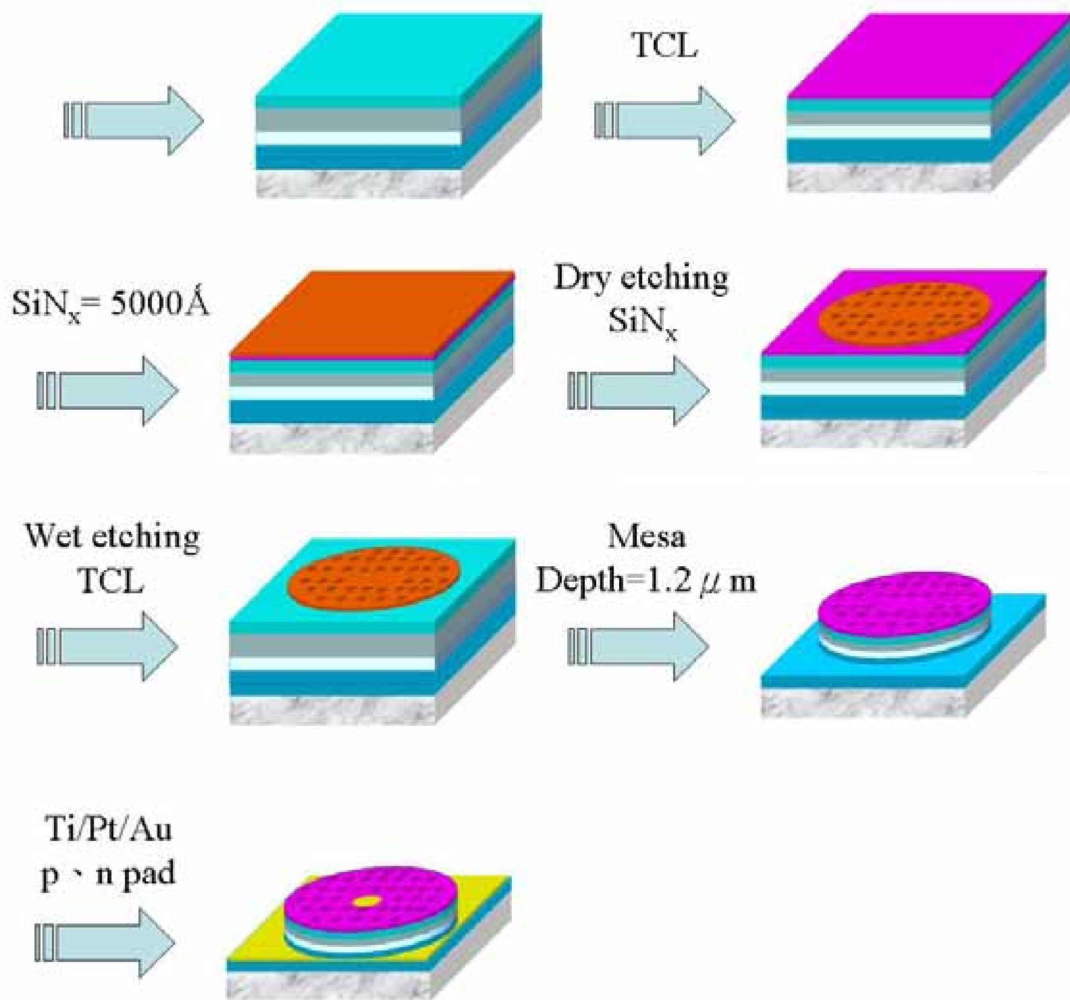

Fig. 5.2 Showing the flowchart of the GaN-based micro-hole array on large-area LEDs by self-aligned process.

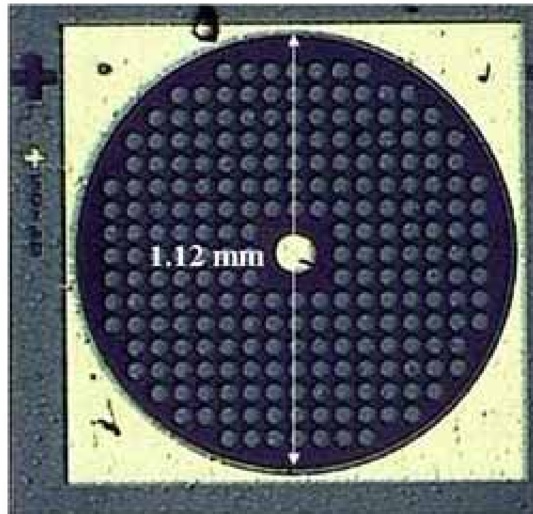

Fig. 5.3. Optical microscope image of micro-hole array on large-area LED with d = 50 μm.

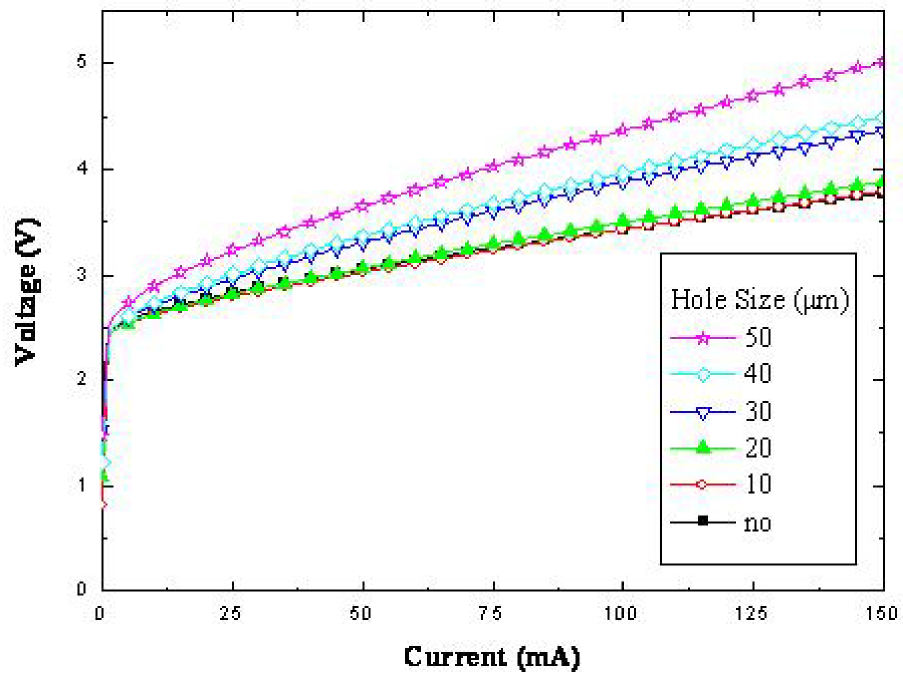

Fig. 5.4. Curves of current-voltage (I-V) of sample A and a conventional BA LED fabricated from the same wafer.

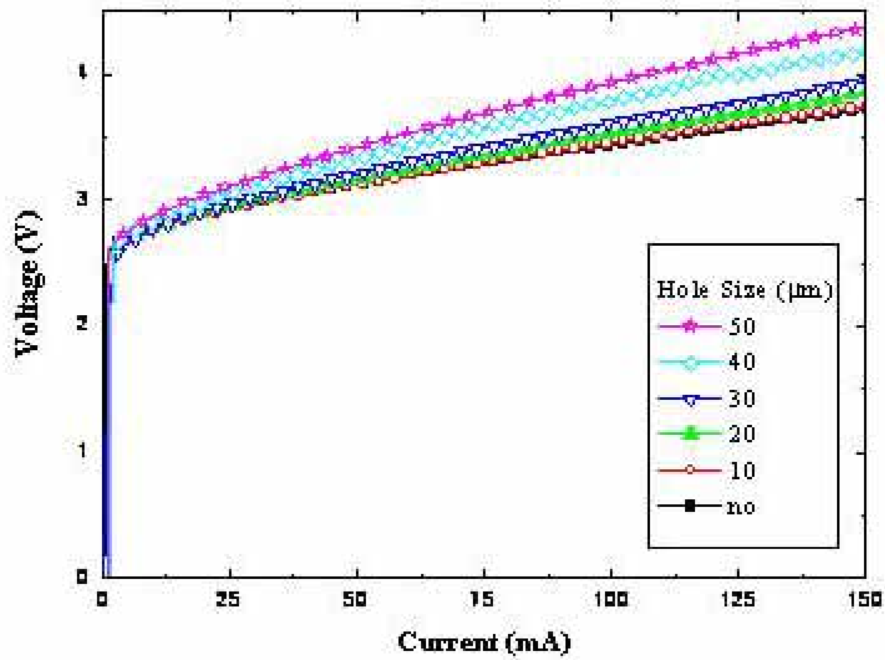

Fig. 5.5. Curves of current-voltage (I-V) of micro-hole array on large-area LEDs and a conventional BA LED fabricated from the same wafer.

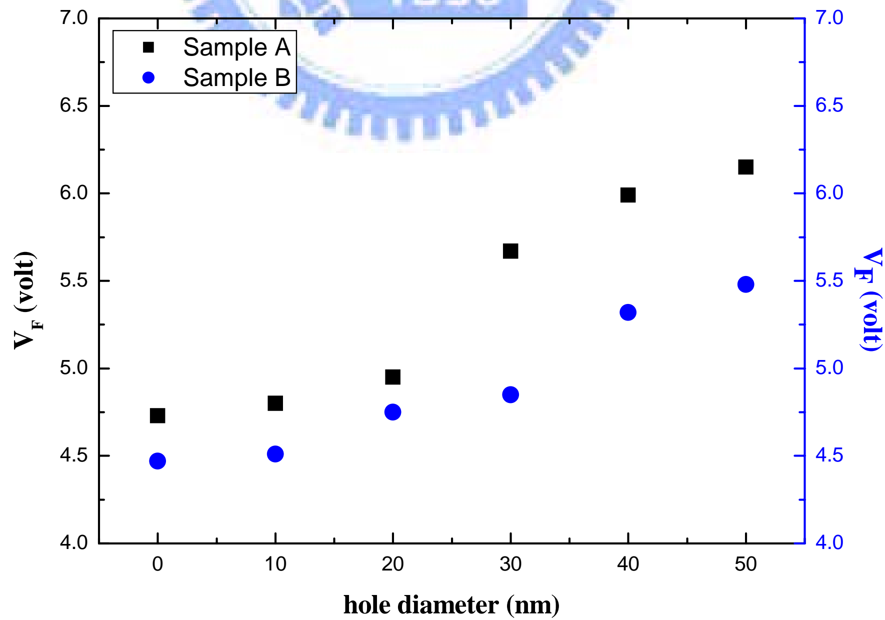

Fig. 5.6. V_F Comparison of sample A and sample B at current= 300 mA .

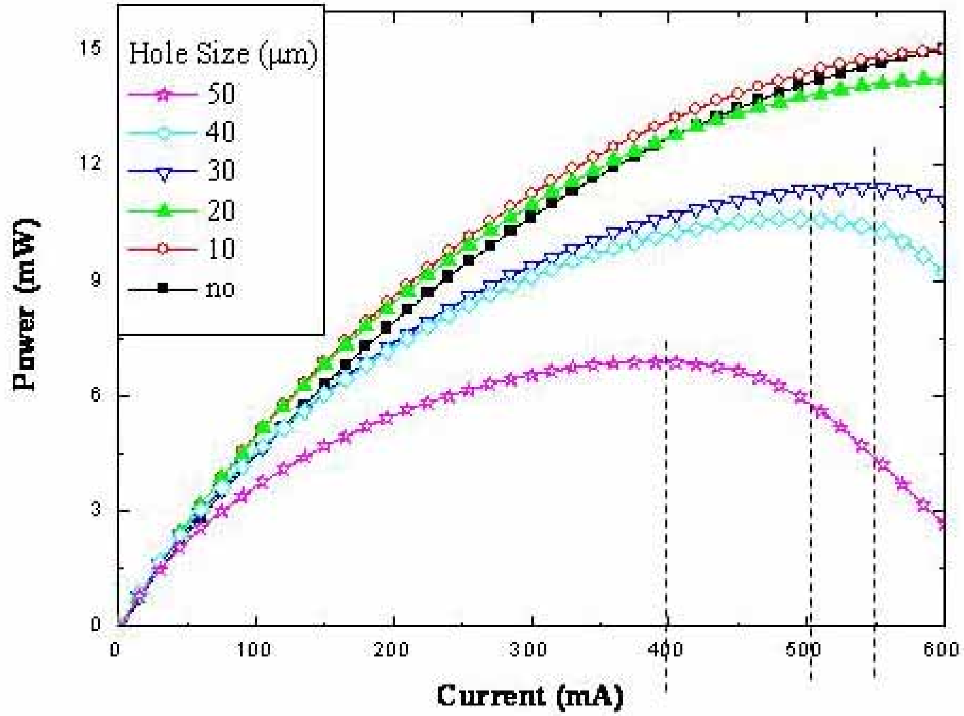

Fig. 5.7. Light output power-current curves of sample A and a conventional BA LED fabricated from the same wafer.

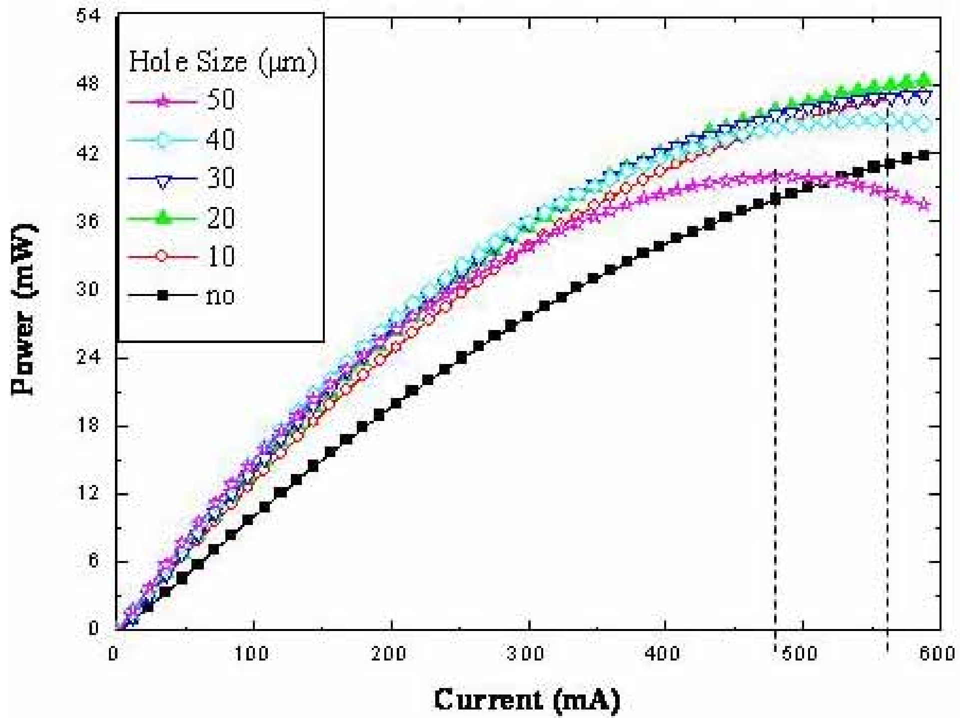

Fig. 5.8. Light output power-current curves of micro-hole array on large-area LEDs and a conventional BA LED fabricated from the same wafer.

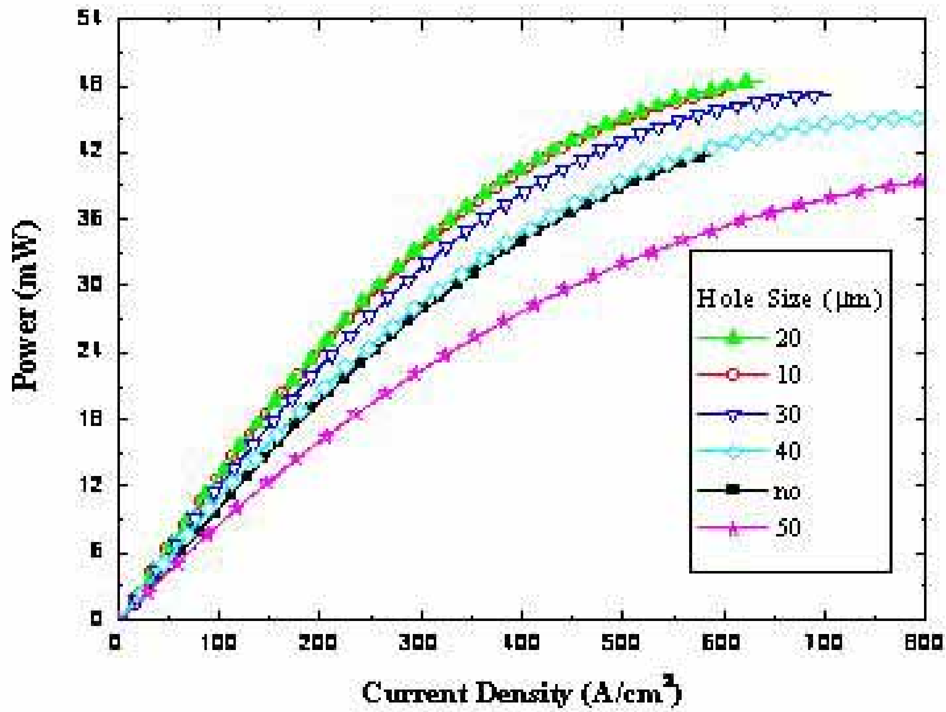

Fig. 5.9. Light output power of micro-hole array LEDs and a conventional BA LED as functions of injected current density.

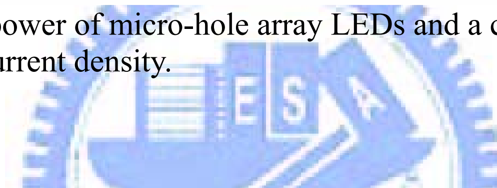

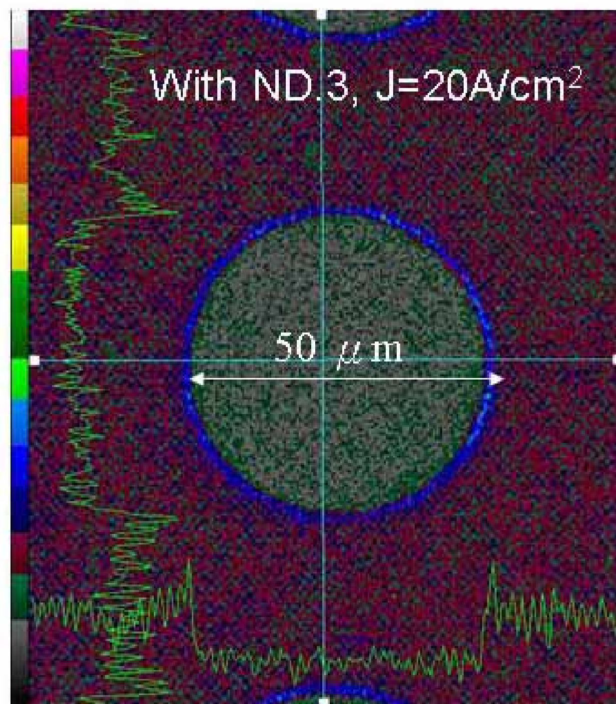

Fig. 5.10. Emission profile of a micro-hole array on large-area LED with d = 50 µm at 20 A/cm^2 driving current.

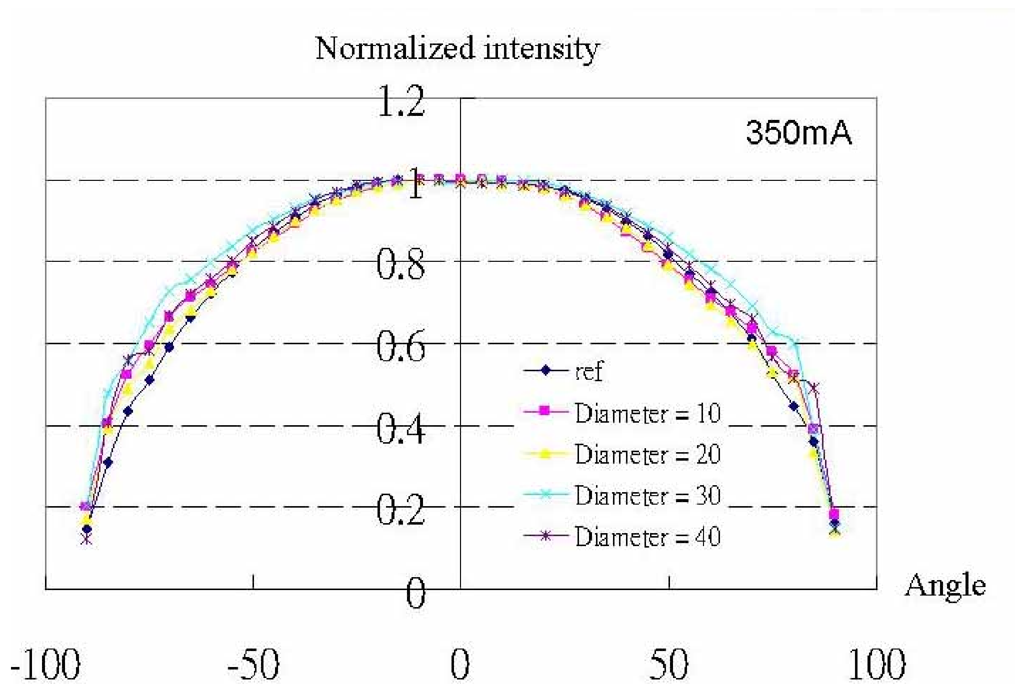

Fig. 5.11. Far field pattern of micro-hole array on large-area LEDs.

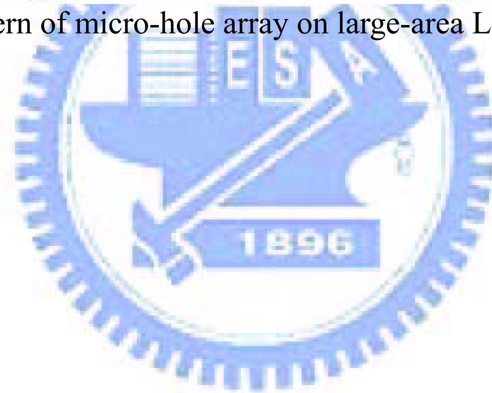

Chapter 6
Conclusion

GaN-based micro-hole array LEDs were fabricated with self-aligned technique. The electrical and light output properties of the micro-hole array LEDs are studied and compared that of the conventional broad-area (BA) LEDs. The forward bias voltage, V_F, of the GaN-based micro-hole array LEDs at a driving current of 20 mA increases with d and slightly exceeds that of the conventional BA LEDs. In the light output characteristics, the enhancement factor of light output from the experimental data decreases as γ increases above 6% ($d > 7$ μm) and no enhancement is observed from the micro-hole array LEDs at $\gamma > 28\%$, which are similar to the simulated results. The light output from the micro-hole array LEDs was over 36% grater than that from conventional LEDs with the same device areas. The increased light output may be due to the competition between the improvement in light extraction and the reduction in the area of the active region while fabricating micro-hole array on LEDs. The optimal design for the GaN-based micro-hole array LEDs are achieved in this work by the experiment and simulation methods.

Furthermore, the optimal design of micro-hole array is used on the GaN-based large-area LEDs. Two kinds of electric conductive material of ITO and Ni/Au are used as the transparent contact layer to the GaN-based large-area micro-hole array LEDs. The results showed that the transparent contact layer of ITO not only decreased the device resistance but also extend the roll-over current. From the emission far-field pattern of LEDs, we found that the micro-hole array on LEDs have little influence on the far field angle. At FWHM, the far field angles are in the range of 75° ~ 80°.

Reference

[1] R. K. Chang and A. J. Campillo, Optical Processes in Microcavities, World Scientific, Singapore (1996).

[2] R. A. Mair, K. C. Zeng, J. Y. Lin, H. X. Jiang, B. Zhang, L. Dai, A. Botchkarev, W. Kim, H. Morkoc, and M. A. Khan, Appl. Phys. Lett. 72, 1530 (1998).

[3] K. C. Zeng, L. Dai, J. Y. Lin, and H. X. Jiang, Appl. Phys. Lett. 75, 2563 (1999).

[4] R. A. Mair, K. C. Zeng, J. Y. Lin, H. X. Jiang, B. Zhang, L. Dai, H. Tang, A. Botchkarev, W. Kim, and H. Morkoc, Appl. Phys. Lett. 71, 2898 (1997).

[5] R. A. Mair, K. C. Zeng, J. Y. Lin, H. X. Jiang, B. Zhang, L. Dai, A. Botchkarev, W. Kim, H. Morkoc, and M. A. Khan, Appl. Phys. Lett. 72, 1530 (1998).

[6] H. X. Jiang, J. Y. Lin, K. C. Zeng, and W. Yang, Appl. Phys. Lett. 75, 763 (1999).

[7] K. C. Zeng, L. Dai, J. Y. Lin, and H. X. Jiang, Appl. Phys. Lett. 75, 2563 (1999).

[8] H. W. Kwok, "Development of liquid crystal on silicon microdisplays," in Proc. 7th Int. Display Workshop, Tokyo, Japan and San Jose, CA, 11-14 (2000).

[9] O. Prache, "Active matrix molecular OLED microdisplays, "Displays, 22, 49 (2001).

[10] C. W. Jeon, H. W. Choi, and M. D. Dawson, IEEE Photonics Tech. Lett. 15, 1516 (2003).

[11] S. X. Jin, J. Li, J. Z. Li, J. Y. Lin, and H. X. Jiang, Appl. Phys. Letts 76, 631 (2000).

[12] H. X. Jiang, S. X. Jin, J. Li, J. Shakya, and J. Y. Lin, Appl. Phys. Lett. 78, 1303 (2001).

[13] H. W. Choi, C. W. Jeon, and M. D. Dawson, IEEE Photonics Tech. Lett. 16, 33 (2004).

[14] C. W. Jeon, H. W. Choi, E. Gu, and M. D. Dawson, IEEE Photonics Technology. Lett. 16, 2421 (2004).

[15] S. X. Jin, J. Li, J. Y. Lin, and H. X. Jiang, Appl. Phys. Lett., 77, 3236, 2000

[16] H. W. Choi, C. W. Jeon, and M. D. Dawson, IEEE Photon. Technol. Lett., 16, 33, (2004.

[17] H. W. Choi, C. W. Jeon, M. D. Dawson, P. R. Edward, R. W. Martin, and S. Tripathy, J. Appl. Phys., 93, 5978, 2003.

[18] R. A. Mair, K. C. Zeng, J. Y. Lin, H. X. Jiang, B. Zhang, L. Dai, H. Tang, A. Botchkarev, W. Kim, and H. Morkoc, Appl. Phys. Lett., 71, 2898, 1997.

[19] K. C. Zeng, L. Dai, J. Y. Lin, and H. X. Jiang, Appl. Phys. Lett., 75, 2563, 1999.

[20] O. Ambacher,W. Rieger, P. Ansmann, H. Angerer, T. D.Moustakas, and M. Stutzmann, Solid State Commun., 97, 365, 1996.

[21] M. y. Broditsk and E. Yablonovitch, in Proc. SPIE, 3002, 119, 1997.

[22] D. Eisert, and V. Harle, International Conference on numerical simulation of semiconductor optoelectronic devices, (2002).

[23] C. C. Kao, H. C. Kuo, H. W. Huang, J. T. Chu, Y. C. Peng, Y. L. Hsieh, C. Y. Luo, and S. C. Wang, C. C. Yu, C. F. Lin, IEEE Photonics Technology Lett. 17, 19 (2005).

[24] J. K. Sheu, G. C. Chi, and M. J. Jou, IEEE Electron Device Lett. 22, 160 (2001).

[25] S. J. Chang, C. S. Chang, Y. K. Su, R. W. Chuang, W. C. Lai, C. H. Kuo, Y. P. Hsu, Y. C. Lin, S. C. Shei, H. M. Lo, J. C. Ke, and J. K. Sheu, IEEE Photonics Technology. Lett. 16, 1002 (2004).

[26] J. K. Sheu, Y. K. Su, G. C. Chi, P. L. Koh, M. J. Jou, C. M. Chang,, C. C. Liu, and W. C. Hung, Appl. Phys. Lett. 74, 2340 (1999).

[27] N. Blanc, P. Gueret, P. Buchmann, K. Datwyler, and P. Vettiger, Appl. Phys. Lett. 56, 2216 (1990).

[28] E. D. Haberer, M. Woods, A. Stonas, C. –H. Chen, S. Keller, M. Hansen, U. Mishra, S. DenBaars, J. Bowers, and E. L. Hu, Mater. Res. Soc. Symp. Proc. 639, G11.21 (2000).

[29] Henrik Wann Jensen. Realistic Image Synthesis using Photon Mapping. AK Peters, 2001.